

**Technical Report
TR-1095**

**Power-Law Scattering Models and
Nonlinear Parametric Estimation for
Super-Resolution Radar**

N. Hatch
D. Holl, Jr.
D. Cyganski

26 April 2004

Lincoln Laboratory
MASSACHUSETTS INSTITUTE OF TECHNOLOGY
LEXINGTON, MASSACHUSETTS



Prepared for the Department of the Air Force under Contract F19628-00-C-0002.

Approved for public release; distribution is unlimited.

ADA427396

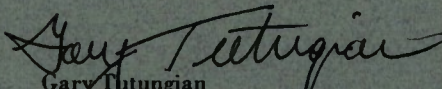
This report is based on studies performed at Lincoln Laboratory, a center for research operated by Massachusetts Institute of Technology. This work was sponsored by the Department of the Air Force, ESC/XPK, under Contract F19628-00-C-0002.

This report may be reproduced to satisfy needs of U.S. Government agencies.

The ESC Public Affairs Office has reviewed this report, and it is releasable to the National Technical Information Service, where it will be available to the general public, including foreign nationals.

This technical report has been reviewed and is approved for publication.

FOR THE COMMANDER


Gary Tutungian
Administrative Contracting Officer
Plans and Programs Directorate
Contracted Support Management

Non-Lincoln Recipients

PLEASE DO NOT RETURN

Permission has been granted to destroy this document, when it is no longer needed.

**Massachusetts Institute of Technology
Lincoln Laboratory**

**Power-Law Scattering Models and Nonlinear Parametric Estimation for
Super-Resolution Radar**

*N. Hatch
D. Holl, Jr.
Group 34*

*D. Cyganski
Worcester Polytechnic Institute*

Technical Report 1095

26 April 2004

Approved for public release; distribution is unlimited.

Lexington

Massachusetts

ABSTRACT

This paper introduces a direct solution of the frequency-dependent, GTD-based, scatterer-model parameters leading towards a new modern spectral-estimation technique to be used for enhanced, super-resolution radar analysis. The overcomplete nature of the full GTD scatterer-model basis (positive and negative half-integer power laws) is recognized and overcome by introducing the vector-channel method, well known from communication theory. This physically motivated discrete-model-based analysis eliminates the need for computationally intensive and potentially nonconvergent local optimization procedures. Each scatterer is assigned a half-integer power law that identifies its cross-section frequency dependence and hence restricts the possible underlying physical feature geometries. This analysis opens the possibility for vector-attribute-based feature processing for target recognition that offers the potential for significant improvement in target identification performance.

TABLE OF CONTENTS

	Page
Abstract	iii
List of Illustrations	vii
List of Tables	ix
 1. INTRODUCTION	 1
 2. BACKGROUND	 3
2.1 Scatterer models	3
2.2 Identifying α	4
 3. PSLI THEORETICAL DEVELOPMENT	 5
3.1 Background: State-space Models and Radar	5
3.2 Direct approach: Structured approximations	9
3.3 Indirect approach: Square-free system models	10
3.4 Negative and fractional power-law estimation	10
3.5 Implementation	13
 4. PERFORMANCE BENCHMARK	 19
4.1 Cramer-Rao Bound	19
4.2 Benchmark Setup	23
4.3 Results	23
 5. STATIC-RANGE DATA	 27
5.1 Ultra-Wideband Analysis	28
5.2 Narrowband Analysis	36
5.3 PSLI Comparison with Fourier and NEM	40
 6. CONCLUSIONS	 51
 APPENDIX A: ADDITIONAL STATIC RANGE RESULTS	 53
A.1 C-Band	53

A.2 X-Band	60
Glossary	67
References	69

LIST OF ILLUSTRATIONS

Figure No.		Page
1	Jordan Normal Form	6
2	Schur Form	7
3	Displacement due to perturbation.	8
4	Dispersion of triple root from unit circle.	8
5	SVD rank reduced approximation of pole location.	11
6	8-ary QPSK-signal space-constellation and symbol-decision regions.	12
7	Example representation of three GTD frequency dependencies	12
8	Cramer-Rao bounds for estimating α over various SNR.	22
9	Cramer-Rao estimation curves for each α	22
10	Benchmark: NEM with 35 dB SNR	24
11	Benchmark: NEM with 15 dB SNR	24
12	Benchmark: PSLI with 35 dB SNR	25
13	Benchmark: PSLI with 15 dB SNR	25
14	Benchmark: NEM and PSLI with 35 dB SNR	26
15	Benchmark: NEM and PSLI with 15 dB SNR	26
16	LL-Cone.	27
17	Frequency dependence of LL-Cone's scattering features.	28
18	X-Band, 4.00 GHz bandwidth, Annotated with scattering feature labels.	29
19	Groove, 4.00 GHz center frequency, 4.00 GHz bandwidth	31
20	Groove, 16.00 GHz center frequency, 4.00 GHz bandwidth	32
21	Groove frequency dependence	33
22	X-Band, 16.00 GHz bandwidth	34
23	X-Band, 4.00 GHz bandwidth, 3D	35
24	X-Band, BW=4.00 GHz, Energy versus aspect angle.	37

25	S-Band, 0.25 GHz bandwidth	38
26	S-Band, 0.50 GHz bandwidth	39
27	S-Band, 0.50 GHz bandwidth, Energy	41
28	S-Band, 0.50 GHz bandwidth, zoomed on the cone tip.	42
29	S-Band, 1.00 GHz bandwidth	43
30	S-Band, 0.50 GHz bandwidth and 15 dB SNR	44
31	Fourier vs. PSLI, S-Band, 1.00 GHz bandwidth, 25 dB SNR	45
32	NEM, S-Band, 2.00 GHz bandwidth	47
33	PSLI, S-Band, 2.00 GHz bandwidth	48
34	NEM 6.50 GHz center frequency, 9.00 GHz bandwidth	49
35	PSLI 6.50 GHz center frequency, 9.00 GHz bandwidth	50
A-1	C-Band, 0.25 GHz bandwidth	54
A-2	C-Band, 0.50 GHz bandwidth	55
A-3	C-Band, 0.50 GHz bandwidth, zoomed on the cone tip.	56
A-4	C-Band, 1.00 GHz bandwidth	57
A-5	C-Band, 0.50 GHz bandwidth, 15 dB SNR	58
A-6	Fourier vs. PSLI, C-Band, 1.00 GHz bandwidth, 25 dB SNR	59
A-7	X-Band, 0.25 GHz bandwidth	61
A-8	X-Band, 0.50 GHz bandwidth	62
A-9	X-Band, 0.50 GHz bandwidth, zoomed on the cone tip.	63
A-10	X-Band, 1.00 GHz bandwidth	64
A-11	X-Band, 0.50 GHz bandwidth, 15 dB SNR	65
A-12	Fourier vs. PSLI, X-Band, 1.00 GHz bandwidth, 25 dB SNR	66

LIST OF TABLES

Table No.		Page
1	GTD-predicted α for various features.	4
2	Speed Comparison: PSLI vs. Fourier & NEM	46

1. INTRODUCTION

In this project, we set out to develop a new modern spectral estimation technique for the enhanced super-resolution radar analysis of frequency-dependent scatterers. We explored classification of frequency dependence based on the geometric theory of diffraction (GTD) based model in which scatterers are taken to have cross sections proportional to the interrogation frequency raised to small positive and negative integer multiples of $\frac{1}{2}$.

Chapter 2 presents general spectral analysis methods as well as radar-scatterer models in the context of GTD. We discuss our theoretical development and disclose our new Parametric Scattering Law Identification (PSLI) algorithm in Chapter 3.

In Chapter 4, we compare PSLI and the alternative algorithm, Nearest Exponential Model (NEM) with respect to performance on synthetic data with reference to the Cramer-Rao bound for frequency-dependence estimation accuracy. In Chapter 5, we compare the GTD models extracted from range data with theoretical predictions. We also note several important features of these models with respect to band center, bandwidth, and angular dependence. Lastly, we summarize our findings and provide conclusions in Chapter 6.

2. BACKGROUND

In this chapter, we will provide the reader with a brief overview of scatterer models used in this analysis, along with a brief introduction to the geometric theory of diffraction (GTD).

2.1 SCATTERER MODELS

This section will present the commonly used scatterer model, along with a natural extension that we shall use for the remainder of this paper. To prepare the reader so that they may better understand the extended model, we shall provide a brief introduction to Keller's GTD.

2.1.1 Traditional Scatterer Model

Traditional analysis assumes that each scatterer takes the form shown in Eq. 1. The scattering strength is represented by A . The round trip phase is represented by $4\pi\frac{fx}{c}$, where x is the range to the scatterer, f is the interrogation frequency, and c is the speed of light [12].

$$s(f) = Ae^{-j4\pi\frac{fx}{c}} \quad (1)$$

Each of the scatterers sum together to create the radar cross section (RCS) of the target for each interrogation frequency.

2.1.2 Extended Scatterer Model: Keller's GTD

Keller [9] introduced the geometric theory of diffraction (GTD) as a means to approximate the RCS of reflectors. GTD assumes the backscattered field originates from a set of discrete scattering centers. The scattering centers also exhibit a frequency dependence proportional to a power-law parameter, f^α , where $\alpha = n/2$ for small positive and negative integers n .

$$s(f) = Af^\alpha e^{-j4\pi\frac{fx}{c}} \quad (2)$$

Potter [15] showed that in practice a broad range of targets acts as a sum of these GTD scatterers. "Creeping waves" that propagate an integer number of times around an object become important for target identification. Table 1 enumerates the α values associated with common features, and Eq. 2 incorporates GTD's power-law parameter, f^α , into the scattering model. Thus, knowledge of a scatterer's power law would significantly aid identification of a target's scattering components. Unfortunately, many existing analysis techniques do not take any frequency dependence into account.

TABLE 1GTD-predicted α for various features.

Scattering Geometries	Power Law
Discontinuity of curvature on edge	$-4/2$
Cone tip	$-2/2$
Curved-edge diffraction	$-1/2$
Doubly curved surface, straight edge	$0/2$
Singly curved surface (cylinder)	$1/2$
Corner reflector, plate	$2/2$
Groove, duct	$3/2$
Rayleigh scattering	$4/2$

2.2 IDENTIFYING α

After having identified the extended model, it is now important to know how to estimate this new power-law parameter, α . We will present some results from an existing technique, the Nearest Exponential Model (NEM) [4], as well as introduce a new technique we call Parametric Scattering Law Identification (PSLI).

As will be shown in Chapter 5, the NEM method was known to work well for narrowband signals, but failed (typically through failure to converge to a solution) with large bandwidth signals. It will also be shown to have a speed disadvantage compared to PSLI since it requires a Newton-Raphson iteration. The PSLI algorithm uses direct solutions to estimate both scatterer position and cross-section parameters, and no iterative computations are required.

3. PSLI THEORETICAL DEVELOPMENT

Is there a basis for generalizing MSA? Can MSA be generalized to tractably yield power-law scatterer components? Why is the MSA problem for exponential models so tractable? Golub and Pereyra [7] identified a general form of problems known as separable nonlinear least squares of which MSA is a special case. This allows the problem to be separated into nonlinear estimation in a few parameters, followed by linear estimation of those remaining. The following sections will show the paths that led us to our final solution to the α estimation problem.

3.1 BACKGROUND: STATE-SPACE MODELS AND RADAR

The radar ranging problem is equivalent to a spectral analysis problem. Some modern spectral analysis (MSA) methods [16] find a linear system with the finite state-space model whose natural response best fits the given data. The complex plane eigenvalues of the state-space model's state-transition matrix (STM)

- identify complex exponentials of the natural response;
- are the roots of the system transfer function;
- are the roots of the STM's characteristic polynomial;
- comprise the range solution of the radar problem.

3.1.1 Positive-integer power systems

This section will discuss the generalized form of the system that analysis of an STM may give. We will first discuss power-law weighted exponentials, along with their state-space models and root multiplicity. We will then describe the problems of handling repeated roots, which include finding a decomposition of defective matrices and root dispersion under perturbation. It will conclude with an overview of ϵ -overcomplete representations.

For purposes of introduction, we will consider briefly the natural response of a continuous-linear time-invariant system since concepts in this environment are often well ingrained from early educational treatment of Laplace transform techniques. These observations map readily into the discrete-frequency domain of radar processing via state-space methods.

The natural response of linear temporal systems with multiple roots in the frequency domain includes terms comprising positive integer power law (PIPL) weighted exponentials:

$$\frac{1}{(s-jb)^{n+1}} \leftrightarrow \frac{1}{n!} t^n e^{jbt}$$

Thus by analogy, identifying PIPL signals from state-space system models involves identifying characteristic polynomial roots or, equivalently, eigenvalues with multiplicity. This implies manipulation and analysis of STMs with repeated eigenvalues which are often “defective” and hence cannot be diagonalized.

Since eigenvalue solvers will either fail or be ill-conditioned, modern, spectral-analysis methods, which are typically based upon eigenanalysis, at present do not address this important case and are ill-behaved when posed with such signals.

3.1.2 Matrix Decompositions for Repeated Roots

The nature of the power-law dependency introduces root multiplicity. Thus, the STM is defective, and commonly used methods to identify eigenvalues are faulty [2]. There are two standard matrix decompositions used for finding eigenvalues with multiplicity, the Jordan normal form (JNF) and the Schur form.

The JNF results from one type of matrix decomposition that may be applied to nondiagonalizable matrices for identifying the eigenvalues and their corresponding algebraic and geometric multiplicities. This is the decomposition, Eq. 3, where P is any matrix. That is, the JNF is the result of a nonunique similarity transform taking A into upper-block diagonal form (J), seen in Eq. 1. The eigenvalues are found on the diagonal.

$$A = PJP^{-1} \quad (3)$$

$$\left[\begin{array}{cccc|ccc} \lambda_1 & 1 & 0 & 0 & & & \\ 0 & \lambda_1 & 1 & 0 & & & \\ 0 & 0 & \lambda_1 & 1 & & & \\ 0 & 0 & 0 & \lambda_1 & & & \\ \hline & & & & \lambda_2 & 1 & 0 \\ & & & & 0 & \lambda_2 & 1 \\ & & & & 0 & 0 & \lambda_2 \end{array} \right]$$

Figure 1. Jordan Normal Form

Eigenvalues in JNF are identified in blocks along the diagonal where the size of the block indicates algebraic multiplicity, and the number of blocks for the same eigenvalue denote geometric multiplicity. For example, Fig. 1 illustrates an example JNF matrix with two eigenvalues, λ_1 and λ_2 , with algebraic multiplicities of 4 and 3, respectively. If $\lambda_1 \neq \lambda_2$, then each has a geometric multiplicity of 1, otherwise, the eigenvalue has geometric multiplicity of 2.

Traditionally, this is not considered a computational option due to poor numerical behavior. We implemented the method described by Kagstom and Ruhe [8] that promised an “accurate and stable algorithm, which computes eigenvalue approximations and chains of principal vectors.” However, we found their method required auspicious choices of problem-dependent, root-clustering parameters.

An alternate matrix decomposition, seen in Eq. 4, is the Schur decomposition.

$$A = PTP^H \quad (4)$$

This is a similarity decomposition, again, where the similarity transformation matrix, P , this time, is a unitary matrix, and the outcome is upper triangular in form. In the resulting upper-triangular matrix T , Eq. 2, the eigenvalues are found on the diagonal. Once again, note that λ_m may equal λ_n for $m \neq n$.

$$\begin{bmatrix} \lambda_1 & ? & ? & ? & ? \\ 0 & \lambda_2 & ? & ? & ? \\ 0 & 0 & \lambda_3 & ? & ? \\ 0 & 0 & 0 & \ddots & ? \\ 0 & 0 & 0 & 0 & \lambda_n \end{bmatrix}$$

Figure 2. Schur Form

It provides numerically stable recovery of eigenvalues whether or not the system is defective or near defective. The JNF provides generalized eigenvectors for any matrix, which are not a direct result of the Schur decomposition, but are not needed to prosecute the state-space model system solution. Hence, Schur method allows the full range of problems to be treated. Demmel [5] provides a comprehensive analysis of both the Jordan and Schur decompositions.

3.1.3 Root Dispersion and Clustering

Noise perturbation of system roots is linear for single roots but is strongly nonlinear for multiple roots [6, 17]. Fig. 3 shows root displacement for a range of perturbations. Note that the slope of the curve approaches infinity as the perturbation approaches zero. This is a general feature of multiple-root dispersion due to perturbation, as a perturbation of size ϵ will perturb an eigenvalue by an amount on the order of $O\left(\epsilon^{\frac{1}{p}}\right)$, where p is the multiplicity of the eigenvalue. Thus, very small perturbations may be expected to have extremely large effects (in comparison to their size) on root locations in the case of multiple roots. In effect, a multiple root will never directly be found for nonrational matrices and nonrational computation simply due to floating-point numerical errors.

Methods have been developed to recover root multiplicity by clustering the perturbed roots [3, 8]. Wilkinson [20] observed that multiple roots of polynomials “explode” symmetrically. The cluster average turns out to be near the original location! This effect is illustrated in Fig. 4, where the signal-to-noise ratio (SNR) is swept from near floating-point precision towards 150 dB. Note that as the noise is increased, the roots explode symmetrically outward.

Unfortunately, these clustering methods are not robust. Clusters and singlet roots due to nearby scatterers cannot be separated. The symmetric explosion only represents the fixed-model order case well.

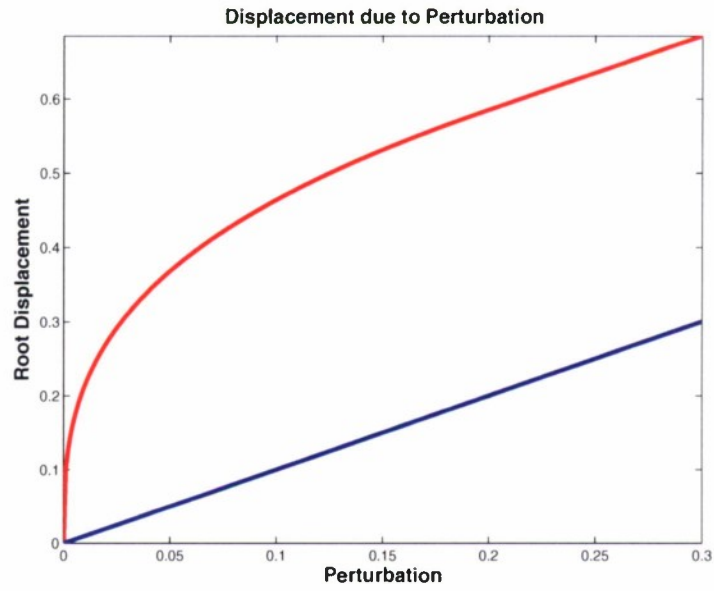


Figure 3. Displacement due to perturbation.

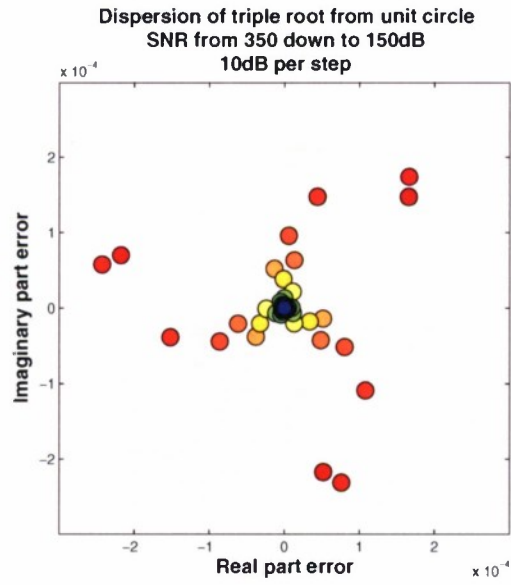


Figure 4. Dispersion of triple root from unit circle.

A multiple-root (PIPL) signal has an exact representation as an infinite sum of decaying exponentials—hence a basis consisting of all root placements, isolated and multiple (equivalent to a basis of exponentially weighted and power-law weighted signals), is overcomplete. **For large, finite data (large bandwidth) the problem is thus ϵ -overcomplete. That is, the basis set possess a Grammian, which approaches zero rapidly as bandwidth increases; hence solutions for representations in this basis become numerically ill-conditioned.**

3.2 DIRECT APPROACH: STRUCTURED APPROXIMATIONS

Another approach to solving the problem of extracting models from perturbed data that maintains a connection to their likely origin as responses described by GTD, is the application of structured approximations. The basic notion is to find a matrix that closely approximates a given STM but also possesses a structure with the desired attribute of having unit magnitude poles with specified multiplicity. Two such methods we investigated included the following:

- Multiple roots of inexact polynomials via pejorative manifolds
- Rank reduction of the Sylvester matrix

3.2.1 Pejorative-Polynomial Manifolds

The objective of this approach is to find roots with models constrained to have multiple roots (pejorative manifolds). “Ill-condition occurs when a polynomial is near a pejorative manifold. If a multiple root is sensitive to small perturbation on the pejorative manifold, then the polynomial is near a pejorative submanifold of higher multiplicity. Ill-condition is caused by solving polynomial equations on a wrong manifold” [22]. For example, given data known to derive from a double-root polynomial:

- Fit a double-root polynomial to the data
Find p so that $x_i^2 + 2px_i + p^2 \approx d_i$
- Rather than trying to group the roots later, find q and r such that

$$x_i^2 + (q + r)x_i + qr \approx d_i$$

then cluster roots p_1 and p_2 that result

The pejorative-manifold process is well-conditioned, but it involves highly nonlinear optimization and it requires knowledge of the initial multiplicity structure. We applied Zeng’s [22] method for computing multiple roots of inexact polynomials. Instead of working on the state matrix directly, this algorithm is applied to the characteristic polynomial of the state matrix. The first stage builds an estimate of the root multiplicity. We found this algorithm to be slow and poorly behaved and to require manipulation of several problem-dependent parameters to obtain convergence.

Another appropriate quote in this case is: “If the answer is highly sensitive to perturbations, you have probably asked the wrong question” [19]. We believe this observation does apply here as does one from Stetter who points out that matrix eigenproblems “represent the weakly nonlinear nucleus to which the original, strongly nonlinear task [of polynomial root finding] may be reduced.” We probably moved in the wrong direction when we converted our matrix analysis problem into a polynomial analysis problem. This will be borne out by our later results.

3.2.2 Structured-matrix projections

This method finds the nearest multiple-root system matrix to that derived from the data matrix. We implemented rank reduction of the Sylvester matrix to find the nearest matrix that has a given number of roots in common with its derivative—the reverse of the square-free polynomial computation.

This method appeared promising but very computationally expensive. We did not pursue this approach beyond proof of concept as it triggered another idea to pursue which becomes the center of the research to be described below.

3.3 INDIRECT APPROACH: SQUARE-FREE SYSTEM MODELS

There is a special property, we discovered, of the truncated SVD for a multiple-root system’s data matrix. SVD rank truncation of the data matrix results in a singlet-root (square-free) system matrix [11]. The new system eigenvalues lie on radials through the original multiple roots. Since all roots were known to originate on the unit circle, they may be reconstructed.

This is a noniterative, robust process for recovery of root locations. In Fig. 5, the circle marks a triple-root location; the solid dots indicate the location of the roots found after matrix perturbation; and the triangle shows our recovered root. After successful root clustering, root multiplicity can be recovered from a linear least-squares auxiliary solution.

3.4 NEGATIVE AND FRACTIONAL POWER-LAW ESTIMATION

This section will describe the problem associated with trying to directly estimate the GTD power law, followed by the path we took to avoid that problem. It introduces the idea of using a PIPL-representation space with GTD-decision regions as a means of avoiding the problem of overcompleteness.

3.4.1 Overcompleteness of a GTD basis

GTD scatterers involve negative and positive multiples of half-power laws. The square-free-system model-based approach fails if a full GTD power-law basis set is introduced into the least-squares problem, because the GTD power-law basis is overcomplete! Yet, this is the natural representation for these problems—how do we obtain the desired model given this situation? The answer lies in that the PIPL power-law set is a complete basis for all system behavior.

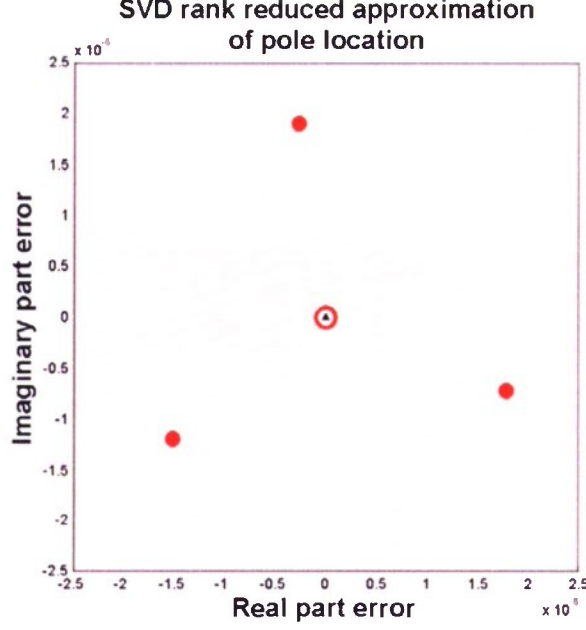


Figure 5. SVD rank reduced approximation of pole location.

3.4.2 Vector-channel model with PIPL basis

The solution to the problem of extracting a full GTD model from only a PIPL decomposition parallels the **M-ary nonorthogonal vector-channel signal-receiver structure**. For example, consider the case of 8-ary QPSK as Fig. 6 depicts. The signalling vector space is divided into decision regions for each of the 8 QPSK symbols, which can be identified despite that the signal space is only two dimensional.

Similarly, the GTD scattering-center power laws can be identified via decision regions in the PIPL-basis space. Fig. 7 shows $a = \frac{1}{2}$ in $a = 0, 1$ basis. Any negative or half-integer power law also yields a unique vector in the multidimensional PIPL space.

3.4.3 PIPL basis as a vector-feature attribute

This technique exploits novel PIPL spectral analysis that is compatible with power-law dependent scatterers. The vector-channel model reduces scattering behavior to one of several well-known GTD-feature types, thus a single degree of freedom. Alternatively, we could use the PIPL-basis vector without reduction to a GTD model, as in a generalized feature attribute with M-degrees of freedom.

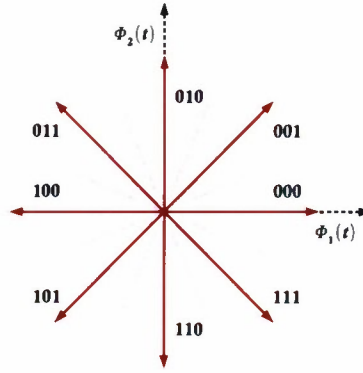


Figure 6. 8-ary QPSK-signal space-constellation and symbol-decision regions.

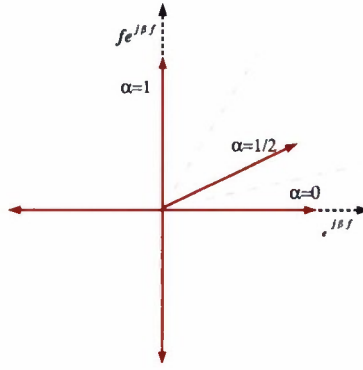


Figure 7. Example representation of three GTD frequency dependencies, f^0 , $f^{\frac{1}{2}}$ and f^1 , in the PIPL-basis space and relevant decision regions for identification of GTD model components from observed PIPL-basis values.

The representation of a scatterer-frequency dependencies in terms of a coefficient vector referencing the PIPL-basis set reveals valuable multispectral information crucial for automatic target recognition (ATR) that would otherwise be obscured by other range-estimation processes. The PIPL-basis representation is closely tied to a Taylor-series expansion of a scatterer's frequency dependence and thus can represent more general relationships than GTD's single-parameter-based f^α identification.

3.5 IMPLEMENTATION

For the implementation of the PSLI technique, we divided the scatterer-identification process into three stages: range estimation, power-law estimation, and amplitude estimation. In short, we use the direct state space (DSS) technique to estimate range (x), decision regions to estimate power law (α), and least squares to estimate scattering amplitudes (A).

At a given target aspect angle, the radar system interrogates the target and returns a collection of reflection coefficients, $\gamma_{1\dots n}$, sampled over a range of interrogation frequencies, $f_{1\dots n}$.

$$f_i = f_1 + (i - 1) \cdot \Delta f \quad (5)$$

$$\gamma_i \triangleq \gamma_{\text{target}}(f_i, \theta, \phi) \quad (6)$$

For convenience, we will use F to denote a vector composed of $f_i \forall i \in (1, n)$, and Γ for the vector composed of $\gamma_i \forall i \in (1, n)$.

$$F = \begin{bmatrix} f_1 \\ \vdots \\ f_n \end{bmatrix} \quad (7)$$

$$\Gamma = \begin{bmatrix} \gamma_1 \\ \vdots \\ \gamma_n \end{bmatrix} \quad (8)$$

3.5.1 Range Estimation

The DSS [10,14] estimator first forms the collected reflection coefficients, γ_i , into a rectangular Hankel $a \times b$ matrix as shown in Eq. 9. The rank of this data matrix represents the number of signals to be estimated in the system. The range to each target is proportional to the angles with respect to the real axis in the eigenspace of the system's STM.

$$\text{Hankel} = \begin{bmatrix} \gamma_1 & \gamma_2 & \cdots & \gamma_b \\ \gamma_2 & \gamma_3 & & \gamma_{b+1} \\ \vdots & & \ddots & \vdots \\ \gamma_a & \gamma_{a+1} & \cdots & \gamma_{a+b-1} \end{bmatrix} \quad (9)$$

The rank (N) of the system may be determined by analyzing the singular-value spectrum. The diagonal elements of Σ represent this spectrum. If there is an estimate of the SNR for the overall radar signal, one may find N by counting the number of singular values that lie above the SNR threshold.

$$\begin{bmatrix} U & \Sigma & V \end{bmatrix} = \text{svd}\{Hankel\} \quad (10)$$

Using the DSS algorithm, we have a choice between two options for computing the STM. We used the observability approach for programming convenience in our particular environment (MATLAB):

- Option 1: Observability Approach

1. Form the observability matrix, \mathcal{O} , from the U and Σ matrices from the SVD.

$$\mathcal{O} = U(:, 1 : N) \cdot \sqrt{\Sigma}(1 : N, 1 : N) \quad (11)$$

2. Form \mathcal{O}_+ and \mathcal{O}_- from \mathcal{O} by deleting the first and last row, respectively.

$$\mathcal{O}_+ = \mathcal{O}(2 : N, :) \quad (12)$$

$$\mathcal{O}_- = \mathcal{O}(1 : N - 1, :) \quad (13)$$

3. Create the STM from the product of the \mathcal{O}_- pseudo-inverse and \mathcal{O}_+ .

$$STM = \mathcal{O}_-^\dagger \cdot \mathcal{O}_+ \quad (14)$$

- Option 2: Controllability Approach

1. Form the controllability matrix, \mathcal{C} , from the Σ and V matrices from the SVD.

$$\mathcal{C} = \sqrt{\Sigma}(1 : N, 1 : N) \cdot V(:, 1 : N)^H \quad (15)$$

2. Form \mathcal{C}_+ and \mathcal{C}_- from \mathcal{C} by deleting the first and last columns, respectively.

$$\mathcal{C}_+ = \mathcal{C}(:, 2 : N) \quad (16)$$

$$\mathcal{C}_- = \mathcal{C}(:, 1 : N - 1) \quad (17)$$

3. Create the STM from the product of \mathcal{C}_+ and the \mathcal{C}_- pseudo-inverse.

$$STM = \mathcal{C}_+ \cdot \mathcal{C}_-^\dagger \quad (18)$$

We use the Schur decomposition to find the STM's eigenvalues, λ_i , and then multiply the angle of these eigenvalues, $\angle\lambda_i$ in Eq. 20, with the scale factor k given in Eq. 19 to produce the range in meters to each scatterer.

$$k = -\frac{c}{4\pi \cdot \Delta f} \quad (19)$$

$$x(i) = k \cdot \angle\lambda_i \quad (20)$$

3.5.2 Power-Law Estimation

The α estimator requires the frequencies (F) used in the interrogation pulse, the eigenvalues of the STM (λ), and the data samples (γ).

We'll first start by defining several notations for convenience. α_i refers to one of the range of possible values specified in Eq. 21 predicted by GTD, and, in Eq. 22, F^{α_i} refers to taking the vector collection of frequencies, F , at which the target was interrogated and raising each element by that α_i .

$$\alpha_{1,2,\dots,9} = \{-2, -1\frac{1}{2}, \dots, 2\} \quad (21)$$

$$F^{\alpha_i} = \begin{bmatrix} f_1^{\alpha_i} \\ \vdots \\ f_n^{\alpha_i} \end{bmatrix} \quad (22)$$

In Eq. 23, we define $\hat{\alpha}_i$ as the collection of power laws in our truncated PIPL basis, and Eq. 24 once again defines the notation $F^{\hat{\alpha}_i}$ to indicate raising each element of our frequency vector, F , by exponent $\hat{\alpha}_i$.

$$\alpha_{\hat{1},2} = \{0, 1\} \quad (23)$$

$$F^{\hat{\alpha}_i} = \begin{bmatrix} f_1^{\hat{\alpha}_i} \\ \vdots \\ f_n^{\hat{\alpha}_i} \end{bmatrix} \quad (24)$$

Our first step is to form an orthonormalized PIPL basis, \mathcal{F} , as depicted in Eq. 25, where Schur decomposition is employed to execute a Gram-Schmidt orthonormalization. We use the GTD-predicted α values to define decision regions within our orthonormalized PIPL space by decomposing F^{α_i} with \mathcal{F} into a library of coefficient vectors, c_{library} .

$$\mathcal{F} = \text{orth} \{ [F^{\alpha_1} \ F^{\alpha_2}] \} \quad (25)$$

$$c_{\text{library}}(i) = \mathcal{F}^\dagger \cdot F^{\alpha_i} \quad (26)$$

Since we are seeking eigenvalues and multiple eigenvalues on the unit circle, admitting no exponentially weighted solutions into our basis set, we denote $\tilde{\lambda}_i$ as STM-pole estimates normalized onto the unit circle in Eq. 27. Then in Eq. 28, we define Λ_i as a matrix whose diagonal is comprised of the pole estimate $\tilde{\lambda}_i$ raised to each element of our frequency vector, F .

$$\tilde{\lambda}_i = \frac{\lambda_i}{|\lambda_i|} \quad (27)$$

$$\Lambda_i = \begin{bmatrix} \tilde{\lambda}_i \frac{f_1}{\Delta f} & 0 & \dots & 0 \\ 0 & \tilde{\lambda}_i \frac{f_2}{\Delta f} & & \vdots \\ \vdots & & \ddots & 0 \\ 0 & \dots & 0 & \tilde{\lambda}_i \frac{f_n}{\Delta f} \end{bmatrix} \quad (28)$$

Our second step to estimating α is to decompose each scatterer's response into our orthonormalized PIPL basis, \mathcal{F} , with the aid of a partitioned matrix, Υ_{PIPL} . As shown in Eq. 29, each partition of Υ_{PIPL} represents the spatial frequency for each target scatterer identified by Λ_i .

$$\Upsilon_{\text{PIPL}} = [\Lambda_1 \cdot \mathcal{F} \mid \Lambda_2 \cdot \mathcal{F} \mid \dots \mid \Lambda_m \cdot \mathcal{F}] \quad (29)$$

Assuming all scatterers have unique ranges, each partition of Υ_{PIPL} ($\Lambda_i \cdot \mathcal{F}$) is separated in spatial frequency, and we can use a pseudo-inverse to decompose the sampled reflection coefficients, Γ , into the partitioned column vector of c_{measured} as shown in Eq. 30.

$$\begin{aligned} c_{\text{measured}} &= \Upsilon_{\text{PIPL}}^\dagger \cdot \Gamma \\ &= \begin{bmatrix} \frac{c_{\text{measured}}(0)}{\vdots} \\ c_{\text{measured}}(m) \end{bmatrix} \end{aligned} \quad (30)$$

The last step to identifying a scatterer's α , is to search for the GTD α_i whose decision library coefficients, $c_{\text{library}}(\alpha_i)$, best match each scatterer's measured basis coefficients, c_{measured} . However, since a scatterer's measured coefficients may have undergone an arbitrary scaling and phase shift, we must first solve for the complex coefficient β . So, for the i^{th} scatterer, we define the scatterer's best α match ($\alpha_{\lambda(i)}$) to be the GTD α_j whose decision-region library vector minimizes Eq. 31.

$$\alpha_{\lambda(i)} \triangleq \alpha_j \quad \text{s.t.} \quad \min_j \left\{ \left\| c_{\text{measured}}(i) - c_{\text{library}}(j) \cdot \underbrace{\left[c_{\text{library}}(j)^\dagger \cdot c_{\text{measured}}(i) \right]}_{\beta} \right\|_2 \right\} \quad (31)$$

3.5.3 Amplitude Estimation

At this point, both range and α have been identified for all scatterers in the system. Now we may use a least-squares system to solve for all scatterer amplitudes simultaneously. In Eq. 32, we create another partitioned matrix, Υ_{GTD} , similar to the one used in Eq. 29. However, now we may use the correct α for each scatterer, $\alpha_{\lambda(i)}$ instead of our orthonormalized PIPL basis when forming each partition¹.

$$\Upsilon_{\text{GTD}} = \left[\Lambda_1 \cdot F^{\alpha_{\lambda(1)}} \mid \Lambda_2 \cdot F^{\alpha_{\lambda(2)}} \mid \dots \mid \Lambda_m \cdot F^{\alpha_{\lambda(m)}} \right] \quad (32)$$

Now using Υ_{GTD} in Eq. 33, we find the least-squared error solution to determine the amplitudes of all scatterers.

$$A = \Upsilon_{\text{GTD}}^\dagger \cdot \Gamma \quad (33)$$

3.5.4 Computational Burden

PSLI's processing speed is dictated by how quickly the three singular value decompositions (SVD $\sim n^3$ computations) in the algorithm may be computed. Equations 34, 35, 36, and 37 approximate the number of required computations, N_{total} , where N_{samples} is the number of interrogated frequencies, $N_{\text{scatterers}}$ is the number of scatterers, and N_{PIPL} is the number of basis vectors ($\hat{\alpha}$) chosen in the implementation.

$$x_{\text{calculations}} \simeq \left[\frac{N_{\text{samples}}^2}{4} \right]^3 \quad (34)$$

$$\alpha_{\text{calculations}} \simeq (N_{\text{samples}} \cdot N_{\text{scatterers}} \cdot N_{\text{PIPL}})^3 \quad (35)$$

$$A_{\text{calculations}} \simeq (N_{\text{samples}} \cdot N_{\text{scatterers}})^3 \quad (36)$$

$$N_{\text{total}} = x_{\text{calculations}} + \alpha_{\text{calculations}} + A_{\text{calculations}} \quad (37)$$

3.5.5 Summary

The process may be summarized as follows. Given the reflection coefficients, Γ , and the frequencies at which the target was interrogated, F , we first find the range to each scatterer using the DSS algorithm. Then, knowing the scatterers' ranges, we decompose Γ into our orthonormal PIPL space to obtain a set of coefficients to be used for matching in decision regions defined by the GTD α library. Finally, with knowledge of the range and α of each scatterer, we solve for the amplitudes by a least-squares fit.

As with most research, there is room for improvement. Eq. 2 incorporates the f^α power-law relationship into the scattering model, and we introduced the PIPL basis to obtain the capability

¹In Υ_{GTD} , each partition consists of a single column.

of generating a generalized multispectral-feature attribute. We could further extend this model to tractably identify an arbitrary response dependent on frequency, aspect angle, and other parameters. For example, a cone requires a four-parameter global optimization: vertex angle, length, and two orientation angles.

4. PERFORMANCE BENCHMARK

This chapter provides an understanding as to how well an unbiased estimator may estimate the frequency-dependent parameter α . It first delves into the theoretical bounds followed by results which compare the performance of the two known algorithms, NEM and PSLI with the Cramer-Rao bound.

4.1 CRAMER-RAO BOUND

This section will present both the derivation of the Cramer-Rao bound (CRB) on parameter estimation performance and its evaluation for various SNRs and α values. “The CRB provides a bound on the covariance matrix of any *unbiased* estimate of $[A, \alpha, \phi, x]$ ” [18]. For simplicity, we only discuss the CRB derivation for the case of a single radar scatterer.

Following Van Trees [18], we start the derivation by defining our signal and adding white Gaussian noise as shown in Eqs. 38 and 39, respectively. In one radar target interrogation, we receive a vector of reflectivity measurements, \tilde{z}_k , taken at each of f_k frequencies and consisting of the original reflected signal, y_k , corrupted with additive white Gaussian noise, \tilde{n}_k . The parameters A , α , x , and ϕ refer to the unknown attributes of a scatterer: amplitude, GTD α , range, and reflection-phase offset, respectively. These unknown parameters are assumed to be real, and $A > 0$.

$$y_k = Af_k^\alpha e^{-4j\pi \frac{xf_k}{c} + \phi j} \quad (38)$$

$$\tilde{z}_k = y_k + \tilde{n}_k \quad (39)$$

In Eq. 40, we describe the probability density function (PDF), $p_{\tilde{z}|A,\alpha,\phi,x}(\tilde{z})$, of \tilde{n}_k as a proper random vector [13], where σ_{noise}^2 is the noise variance.

$$p_{\tilde{z}|A,\alpha,\phi,x}(\tilde{z}) = \prod_{k=0}^{N-1} \frac{1}{\pi\sigma_{noise}^2} e^{-(z_k - y_k)^H (z_k - y_k) / \sigma_{noise}^2} \quad (40)$$

As shown in Eq. 41, we next need to find the natural logarithm of our PDF, $L_{\tilde{z}}(A, \alpha, \phi, x)$. This function is sometimes referred to as the *log-likelihood function*.

$$\begin{aligned} L_{\tilde{z}}(A, \alpha, \phi, x) &\triangleq \ln p_{\tilde{z}|A,\alpha,\phi,x}(\tilde{z}) \\ &= -N \ln(\pi\sigma_{noise}^2) - \frac{1}{\sigma_{noise}^2} \sum_{k=0}^{N-1} (z_k - y_k)^H (z_k - y_k) \\ &= -N \ln(\pi\sigma_{noise}^2) - \frac{1}{\sigma_{noise}^2} \sum_{k=0}^{N-1} \Re^2(z_k - y_k) + \Im^2(z_k - y_k) \end{aligned} \quad (41)$$

$$\begin{aligned}
= & -N \ln(\pi \sigma_{noise}^2) - \frac{1}{\sigma_{noise}^2} \left[A^2 f_k^{2\alpha} + \Im(z_k)^2 + \Re(z_k)^2 \quad \dots \right. \\
& + \sum_{k=0}^{N-1} 2A f_k^\alpha \Im(z_k) \sin\left(4\pi \frac{x f_k}{c} - \phi\right) \quad \dots \\
& \left. - \sum_{k=0}^{N-1} 2A f_k^\alpha \Re(z_k) \cos\left(4\pi \frac{x f_k}{c} - \phi\right) \right]
\end{aligned}$$

To compute the Cramer-Rao bound, we form *Fisher's information matrix* (FIM) by finding the Hessian of $L_{\bar{z}}(A, \alpha, \phi, x)$ with respect to A , α , ϕ and x .

$$\mathbb{F} = -E\{H L_{\bar{z}}(A, \alpha, \phi, x)\} \quad (42)$$

$$\begin{aligned}
& = -E \left\{ \begin{pmatrix} \frac{\partial^2}{\partial A^2} & \frac{\partial^2}{\partial A \partial \alpha} & \frac{\partial^2}{\partial A \partial \phi} & \frac{\partial^2}{\partial A \partial x} \\ \frac{\partial^2}{\partial \alpha \partial A} & \frac{\partial^2}{\partial \alpha^2} & \frac{\partial^2}{\partial \alpha \partial \phi} & \frac{\partial^2}{\partial \alpha \partial x} \\ \frac{\partial^2}{\partial \phi \partial A} & \frac{\partial^2}{\partial \phi \partial \alpha} & \frac{\partial^2}{\partial \phi^2} & \frac{\partial^2}{\partial \phi \partial x} \\ \frac{\partial^2}{\partial x \partial A} & \frac{\partial^2}{\partial x \partial \alpha} & \frac{\partial^2}{\partial x \partial \phi} & \frac{\partial^2}{\partial x^2} \end{pmatrix} L_{\bar{z}}(A, \alpha, \phi, x) \right\} \\
& = \begin{pmatrix} \mathbb{F}_{1,1} & 0 \\ 0 & \mathbb{F}_{2,2} \end{pmatrix}
\end{aligned}$$

$$\mathbb{F}_{1,1} = \begin{pmatrix} \frac{2}{\sigma^2} \sum_{k=0}^{N-1} f_k^{2\alpha} & \frac{2A}{\sigma^2} \sum_{k=0}^{N-1} f_k^{2\alpha} \ln(f_k) \\ \frac{2A}{\sigma^2} \sum_{k=0}^{N-1} f_k^{2\alpha} \ln(f_k) & \frac{2A^2}{\sigma^2} \sum_{k=0}^{N-1} f_k^{2\alpha} \ln(f_k)^2 \end{pmatrix} \quad (43)$$

$$\mathbb{F}_{2,2} = \begin{pmatrix} \frac{2A^2}{c^2 \sigma^2} \sum_{k=0}^{N-1} f_k^{2\alpha} & \frac{8A^2 \pi}{c^2 \sigma^2} \sum_{k=0}^{N-1} f_k^{2\alpha+1} \\ \frac{8A^2 \pi}{c^2 \sigma^2} \sum_{k=0}^{N-1} f_k^{2\alpha+1} & \frac{32A^2 \pi^2}{c^2 \sigma^2} \sum_{k=0}^{N-1} f_k^{2\alpha+2} \end{pmatrix} \quad (44)$$

Lastly, we take the inverse of \mathbb{F} to obtain the CRB's covariance matrix, \mathbb{C} , in Eq. 45. The diagonal of \mathbb{C} gives the optimal bounds on estimation variance for the unknown scatterer parameters, σ_A^2 , σ_α^2 , σ_ϕ^2 , and σ_x^2 in Eq. 46, which are given in Equations 47, 48, 49 and 50, respectively.

$$\mathbb{C} = \mathbb{F}^{-1} \quad (45)$$

$$\begin{aligned}
& = \begin{pmatrix} \mathbb{C}_{1,1} & \mathbb{C}_{1,2} & 0 & 0 \\ \mathbb{C}_{2,1} & \mathbb{C}_{2,2} & 0 & 0 \\ 0 & 0 & \mathbb{C}_{3,3} & \mathbb{C}_{3,4} \\ 0 & 0 & \mathbb{C}_{4,3} & \mathbb{C}_{4,4} \end{pmatrix} \\
\{\sigma_A^2, \sigma_\alpha^2, \sigma_\phi^2, \sigma_x^2\} & \triangleq \text{diag}\{\mathbb{C}\} \\
& = \{\mathbb{C}_{1,1}, \mathbb{C}_{2,2}, \mathbb{C}_{3,3}, \mathbb{C}_{4,4}\}
\end{aligned} \quad (46)$$

$$\sigma_A^2 = \frac{1}{2} \frac{\sigma_{noise}^2 \sum_{k=0}^{N-1} f_k^{2\alpha} \ln(f_k)^2}{\left(\sum_{k=0}^{N-1} f_k^{2\alpha} \ln(f_k)^2 \right) \left(\sum_{k=0}^{N-1} f_k^{2\alpha} \right) - \left(\sum_{k=0}^{N-1} f_k^{2\alpha} \ln(f_k) \right)^2} \quad (47)$$

$$\sigma_\alpha^2 = \frac{1}{2} \frac{\sigma_{noise}^2 \sum_{k=0}^{N-1} f_k^{2\alpha}}{A^2 \left(\left(\sum_{k=0}^{N-1} f_k^{2\alpha} \ln(f_k)^2 \right) \left(\sum_{k=0}^{N-1} f_k^{2\alpha} \right) - \left(\sum_{k=0}^{N-1} f_k^{2\alpha} \ln(f_k) \right)^2 \right)} \quad (48)$$

$$\sigma_\phi^2 = \frac{1}{2} \frac{\sigma_{noise}^2 \sum_{k=0}^{N-1} f_k^{2\alpha+2}}{A^2 \left(\left(\sum_{k=0}^{N-1} f_k^{2\alpha+2} \right) \left(\sum_{k=0}^{N-1} f_k^{2\alpha} \right) - \left(\sum_{k=0}^{N-1} f_k^{2\alpha+1} \right)^2 \right)} \quad (49)$$

$$\sigma_x^2 = \frac{1}{32} \frac{\sigma_{noise}^2 c^2 \sum_{k=0}^{N-1} f_k^{2\alpha}}{A^2 \pi^2 \left(\left(\sum_{k=0}^{N-1} f_k^{2\alpha+2} \right) \left(\sum_{k=0}^{N-1} f_k^{2\alpha} \right) - \left(\sum_{k=0}^{N-1} f_k^{2\alpha+1} \right)^2 \right)} \quad (50)$$

Upon inspection of Eq. 48, we note that the CRB for α estimation is inversely proportional to the SNR, and it also asymptotically improves as inverse bandwidth. We illustrate these relationships in Fig. 8, which plots the α estimation standard deviation (σ_α) for various SNRs from 25 dB to -15 dB. From GTD, α must be a small positive or negative integer multiple of $\frac{1}{2}$, so we can define a soft measure where we assume we may obtain useful α estimates when the standard deviation, σ_α , is less than about $\frac{1}{4}$.

Noteworthy is that Fig. 8 plots σ_α assuming the true α equals zero. Other curves are not shown here or later because we found little difference between error curves for the different GTD α values. This fact is made evident by Fig. 9 in which a plot appears of the *difference in σ_α relative to $\alpha = 0$* for various values of α .

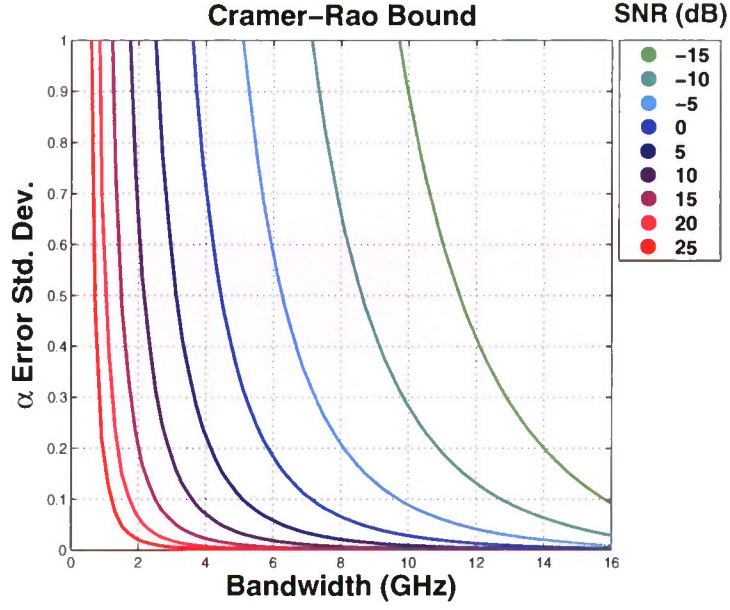


Figure 8. Cramer-Rao bounds for estimating α over various SNR.

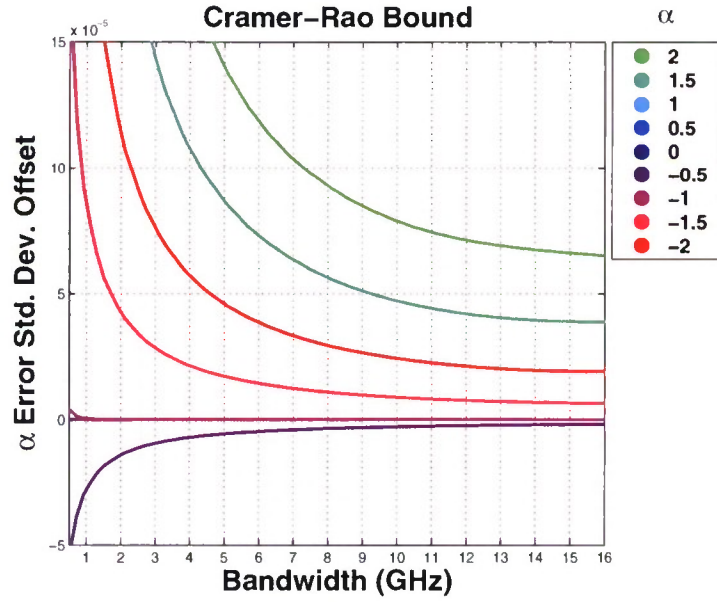


Figure 9. Difference between Cramer-Rao estimation-performance bounds for various α and that of $\alpha = 0$.

4.2 BENCHMARK SETUP

It was desired to know how well the PSLI algorithm performed when compared to both the Cramer-Rao unbiased estimator bounds as well as to the NEM algorithm. A benchmark was configured that used a single scatterer with various α 's. The RCS of this single scatterer was then analyzed using each method while varying the bandwidth (0.5–17 GHz) and the SNR (0–60 dB). Knowing the truth signal, we then plotted the standard deviation of the difference between experimental and truth values vs. bandwidth for each SNR. As will be seen, we found that the NEM estimators ability to correctly identify the frequency dependence deteriorates when the bandwidth is increased, while the PSLI estimator correctly identifies the frequency dependence for narrow through ultra-wide bandwidths.

4.3 RESULTS

4.3.1 Nearest Exponential Model (NEM)

The NEM method was developed by Cuomo, et al., at MIT Lincoln Laboratory [4]. In effect, a global all-pole signal model is optimally fit to the measured data. The approach determines the all-pole model parameters that minimize a particular cost function using Newton Raphson iteration.

Figures 10 and 11 show NEM's performance at 35 dB and 15 dB SNR, respectively. With 35 dB SNR, the NEM method performs well until the bandwidth reaches about 4 GHz, at which point the error slopes upward for all α values. With a SNR of 15 dB, the NEM algorithm performs reasonably well until the bandwidth exceeds approximately 7 GHz to 8 GHz.

4.3.2 Parametric Scattering Law Identification (PSLI)

In Figures 12 and 13, the PSLI algorithm demonstrates similar error performance to NEM for small bandwidths, but improves noticeably with increased bandwidth or SNR. In both cases of 35 dB and 15 dB SNR, the PSLI's error approaches zero for large bandwidths, as opposed to the NEM method, which degrades.

4.3.3 PSLI vs. NEM

Figures 14 and 15 give a side-by-side comparison of the NEM and PSLI algorithms for wider bandwidths. It can be seen in both figures that only the PSLI estimate reaches zero error for increasing bandwidth, while the NEM algorithm's performance deteriorates beyond a bandwidth of approximately 4 GHz. We attribute the lower performance for high SNR and low bandwidth of NEM to suspected failure of internal eigenanalysis for clusters of roots too close to admit to usual approach.

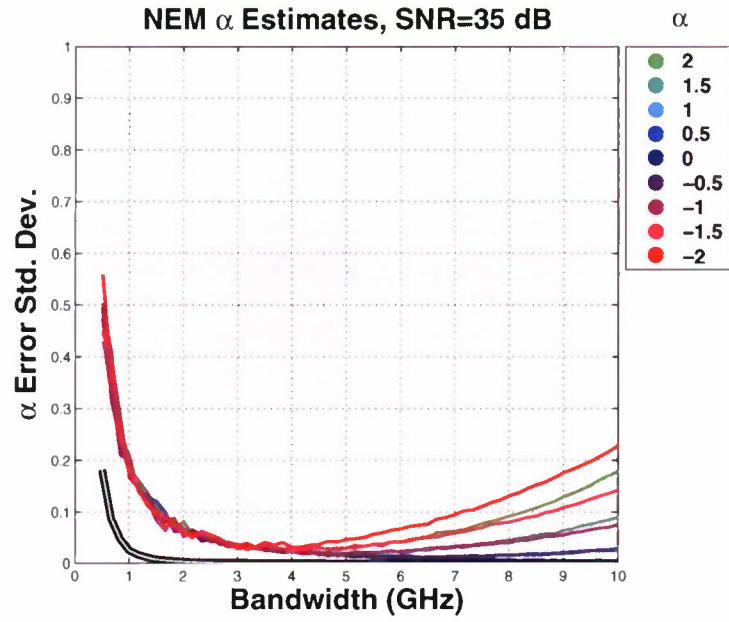


Figure 10. Benchmark: NEM with 35 dB SNR

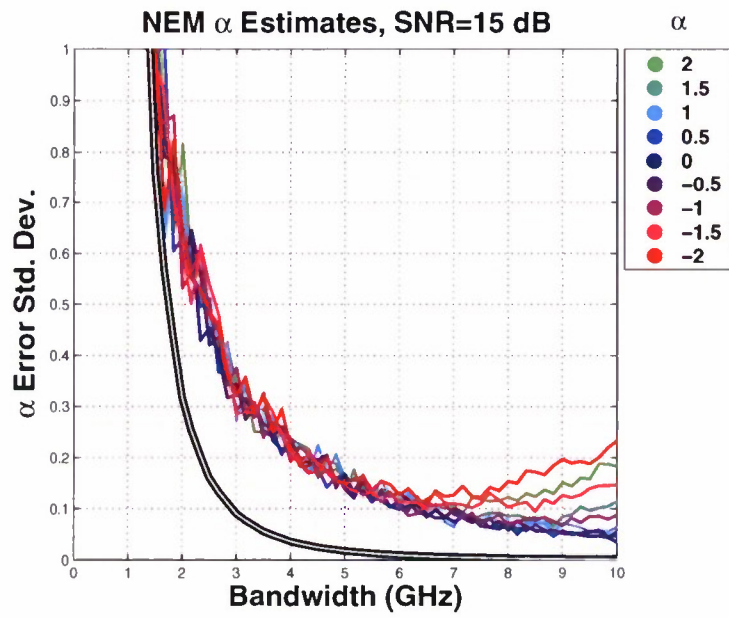


Figure 11. Benchmark: NEM with 15 dB SNR

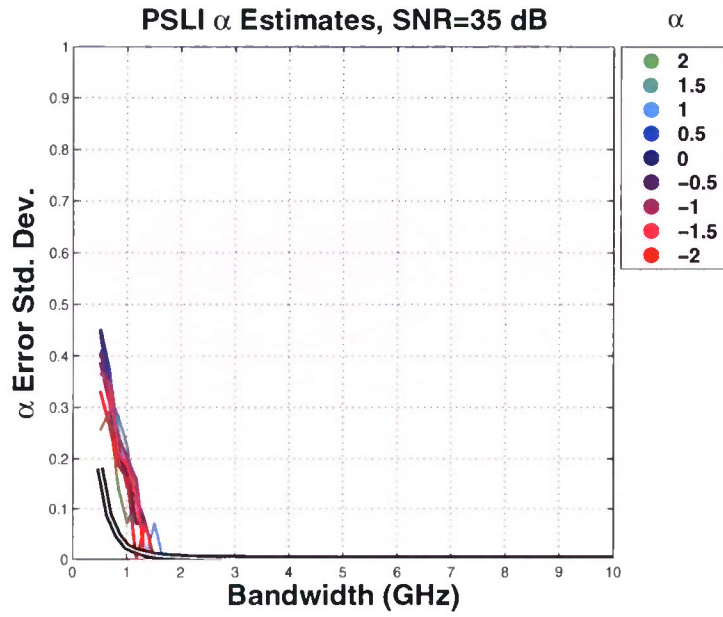


Figure 12. Benchmark: PSLI with 35 dB SNR

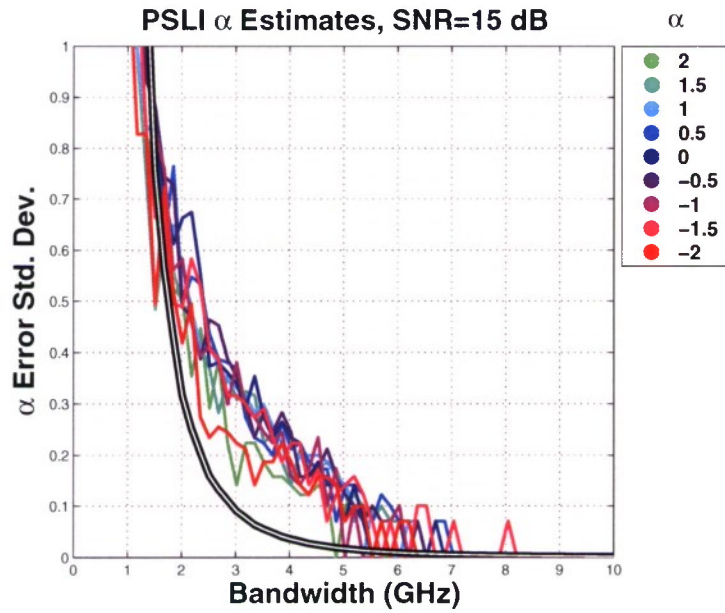


Figure 13. Benchmark: PSLI with 15 dB SNR

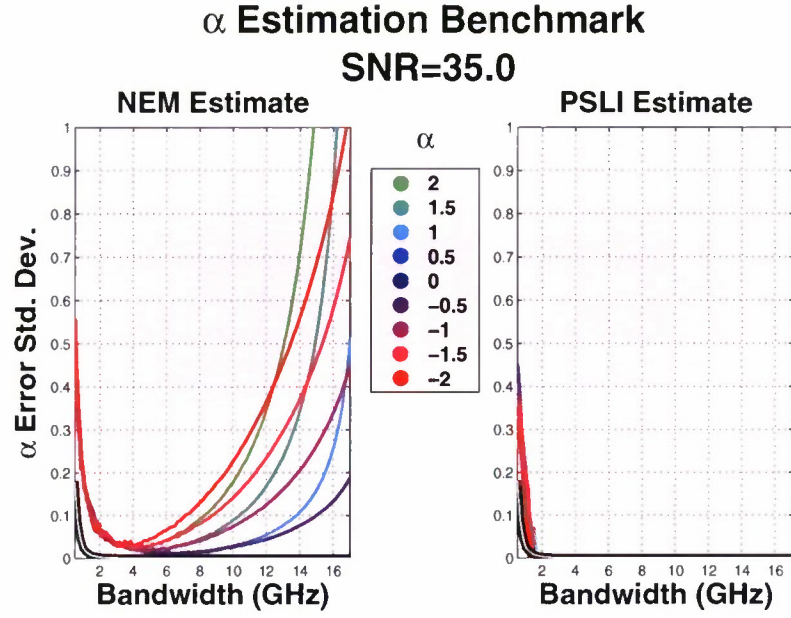


Figure 14. Benchmark: NEM and PSLI with 35 dB SNR

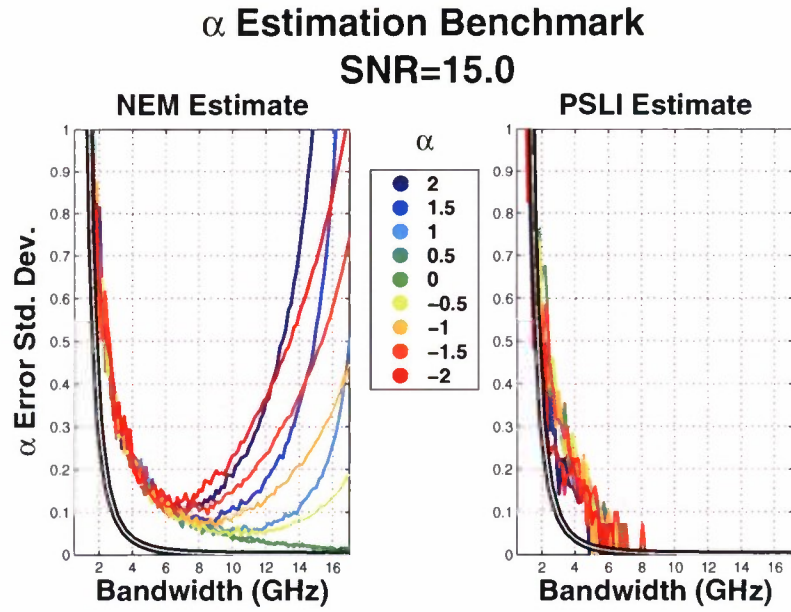


Figure 15. Benchmark: NEM and PSLI with 15 dB SNR

5. STATIC-RANGE DATA

Synthetic data is sufficient for benchmark comparisons such as described in the last chapter, however actual radar data is needed to determine if the results are useful within the context of valuable targets.

The target referred to as LL-Cone was used for many of our tests. The radar data samples for the 1.6 m long target, LL-Cone, were collected at Point Mugu. The data set contains frequency samples from 2 to 18 GHz with 20 Mhz sample spacing, taken for 360° of aspect angle with 0.1 degree sample spacing. We chose to use the horizontally transmitted, horizontally received (HH) polarization because certain features were simpler to analyze for this polarization set.



Figure 16. LL-Cone.

A detailed specification for this object was provided by Lincoln Laboratory [21]. This target has also been analyzed in the past using ESPRIT by Michael Burrows at Lincoln Laboratory [1].

Since the dataset has 16 GHz bandwidth, it allows for narrowband through ultra-wideband analysis. The RCS data set was collected in a controlled environment, thus giving it a high SNR. The frequency-dependence parameter α will be seen to be a function of scattering phenomenology, frequency range, and scattering angle. Scatterers and their power laws can be connected to features on the target. This frequency dependence may provide strong clues as to the identity of the target.

Regarding most future figures, if there is an α legend with a plot, then plot color denotes the α parameter. If there is a colorbar with a plot, then the plot color denotes energy, not α . To read the various LL-Cone plots, please note that at the azimuth angle of 0° the cone tip is pointing towards the radar.

While many features can be identified in each plot, it may be helpful to begin interpretation with the following information about key features: We predict, according to GTD (Table 1), the nose tip will have an alpha of 0; the 3 grooves have one of $3/2$; and the base edges are $-1/2$ at S-band. These features will be described in greater detail below. These GTD predictions for LL-Cone's power laws are shown in Fig. 17.

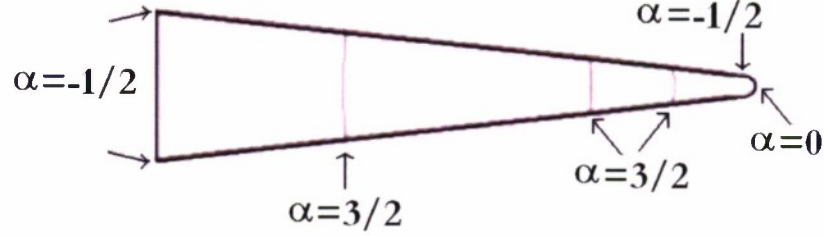


Figure 17. Frequency dependence of LL-Cone's scattering features.

5.1 ULTRA-WIDEBAND ANALYSIS

This section discusses an ultra-wideband analysis of LL-Cone using bandwidths of 4 GHz and 16 GHz respectively, sampled at 20 MHz steps² at X-band³. We will first present the 4-GHz-bandwidth analysis and then the analysis for 16 GHz.

Using PSII, we created the plot of scattering-feature range versus target-aspect angle shown in Fig. 18. This analysis of LL-Cone used 4 GHz bandwidth, and we color coded each scatterer by its estimated GTD power law (α). Although not specifically marked in the figure, scattering-energy estimates were used to fade each scatterer's color to provide a sense of reflectivity. We will elaborate on PSII's energy estimates later with Fig. 23 (page 35) and Fig. 24 (page 37). Also, to assist with the discussion in the next few paragraphs, we annotated Fig. 18 with some of LL-Cone's more prominent features.

At an aspect angle of -180° and range of -0.88 m in Fig. 18, PSII identifies LL-Cone's base edges with a purple shade to indicate the estimate power law $\alpha = -\frac{1}{2}$. The base edges cross at -180° , because, when the bottom of the cone is pointing towards the radar system, both bases are at an equal range (-0.88 m). As the cone tip is rotated towards the radar system, the two base edges move apart from one another until they meet the maximum distance of the base length near $\pm 90^\circ$ and 0.1 m. One of the base edges is shadowed by the rest of the target until $\sim \pm 10^\circ$, where the cone tip is pointing towards the radar. At this point the visible base edge becomes shadowed, and the shadowed base edge becomes visible.

²At 20 MHz between frequency samples, 4 GHz \sim 201 frequency samples, and 16 GHz \sim 801 frequency samples.

³X-band processing center frequency is 10 GHz.

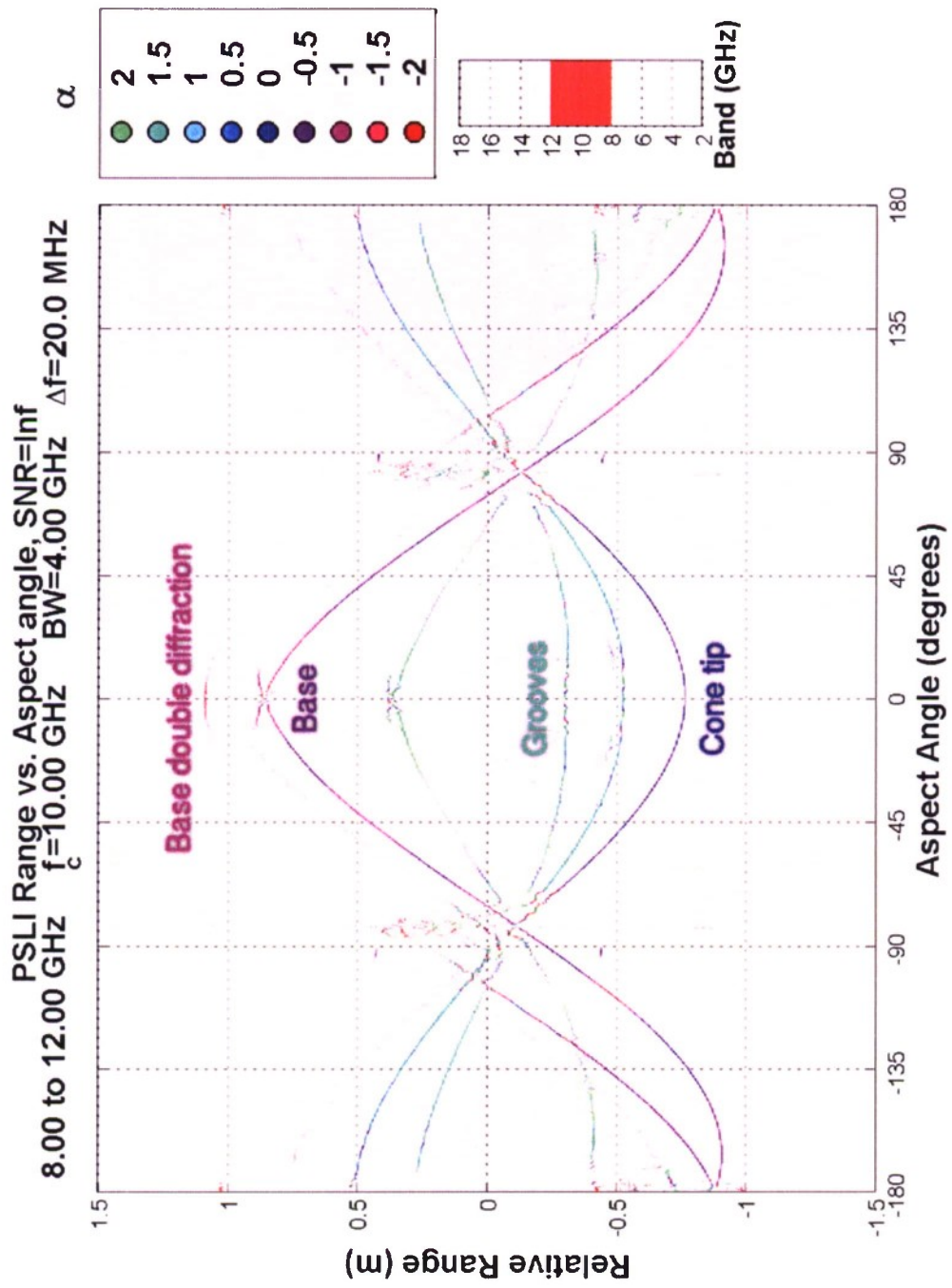


Figure 18. X-Band, 4.00 GHz bandwidth, Annotated with scattering feature labels.

Also in Fig. 18, another feature predicted by GTD is the cone tip's power law changes with aspect angle. At 0° and -0.765 m, the tip's GTD power law is $\alpha = 0$, which, because the cone tip is spherical, agrees with GTD's prediction that spheres have an α of 0 (Table 1). At aspect angles to either side of 0° , the cylindrical nature of the geometry due to the transition from hemisphere to cone dominates. This cylindrical form causes the α to transition to $\frac{1}{2}$, as shown in Table 1.

Fig. 19 presents the PSLI analysis centered at 4 GHz, and, in it, we identify the first groove as the track passing through range -0.52 m at 0° . Note that at 0° , it is attributed with $\alpha = \frac{3}{2}$ as would be expected of a groove according to GTD predictions (Table 1). However, for aspect angles approaching 3° the value of alpha changes. This can be attributed to interaction of the groove with travelling waves on the cone surface that become more prominent at certain illumination angles.

In Fig. 20, which is based on the data with a higher center frequency, 16 GHz, we see the α assigned to this feature has changed to average value of $-\frac{1}{2}$. This does not result from any failure of the PSLI method at wider bandwidths, but rather results from the fact that the frequency dependence of a feature is not constant over large ranges of frequency. This is amply demonstrated by the graph in Fig. 21 from Cuomo, et al., where we see the first groove's α sweeping from $\frac{3}{2}$ down to $-\frac{1}{2}$. Note that the estimated power law versus aspect angle has greater variation at this center frequency of 16 GHz than at the center frequency of 4 GHz. We attribute this to resonance occurring at the higher frequencies.

Thus in the wider, 16-GHz-bandwidth plot of Fig. 22, we see that PSLI has estimated the first groove's frequency dependence to be the average of the values attained over the range described by Fig. 21. Of course, this represents a loss of information about the target as the particulars of the change of frequency dependence are completely determined by geometric features of not just the groove but also by the global geometry of the entire target. **In Section 3.4.3, we discuss how PSLI offers a means to extract a more complete polynomial model of the entire frequency-dependence curve. This generalized ability could be used to provide valuable advanced attribute-feature information to automatic target recognition (ATR) schemes as the current example demonstrates.**

As predicted by GTD and described above, a scatterers α changes versus frequency. For a given frequency, the α variation over aspect angle can aid in target identification. The resonances that occur and the aspect angles at which they occur again leads to the body of information that can be used to identify a target. For many of the bandwidths for which we show results, the second and third grooves, found starting at -170° and both 0.265 m and -0.4 m, respectively, maintain the same power law of $\alpha = \frac{3}{2}$, aside from slight resonances that occur. This α value is predicted by GTD for grooves (Table 1).

To illustrate some results from more complex scattering mechanisms, we note that both Figures 18 and 22 also contain an example of wave diffraction around the *back* of LL-Cone. At 0° aspect angle and 1.08 m, one can see the double-scattering curves across the base. This is caused by the wavefront hitting the cone at one base edge, inducing a travelling wave across the base, which then scatters back from the other base edge. We can clearly make the association of double scattering with the α estimates in that two $-1/2$ alpha scattering events do indeed add up to a -1 attribution of the double-scattering track.

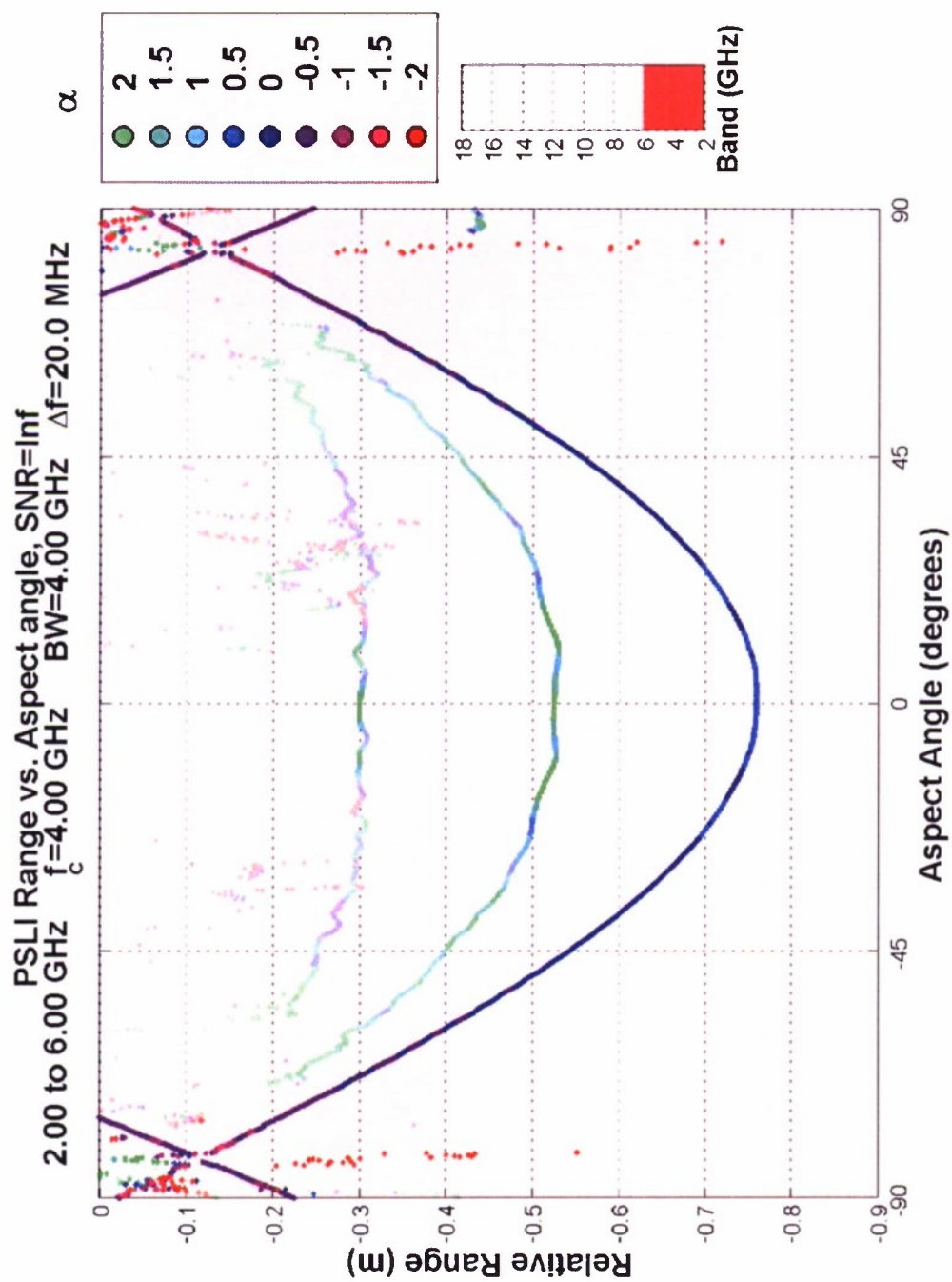


Figure 19. Groove, 4.00 GHz center frequency, 4.00 GHz bandwidth

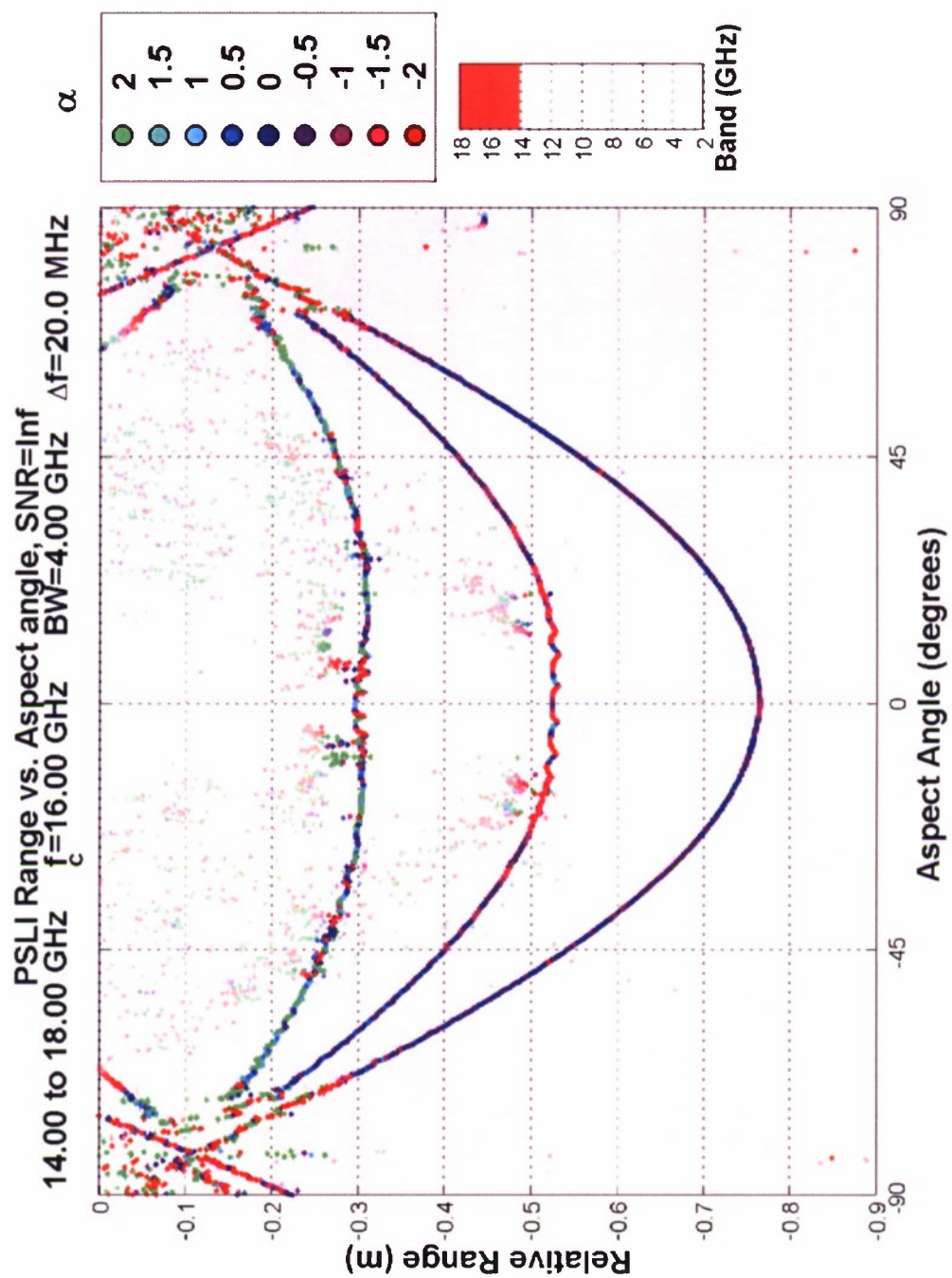


Figure 20. Groove, 16.00 GHz center frequency, 4.00 GHz bandwidth

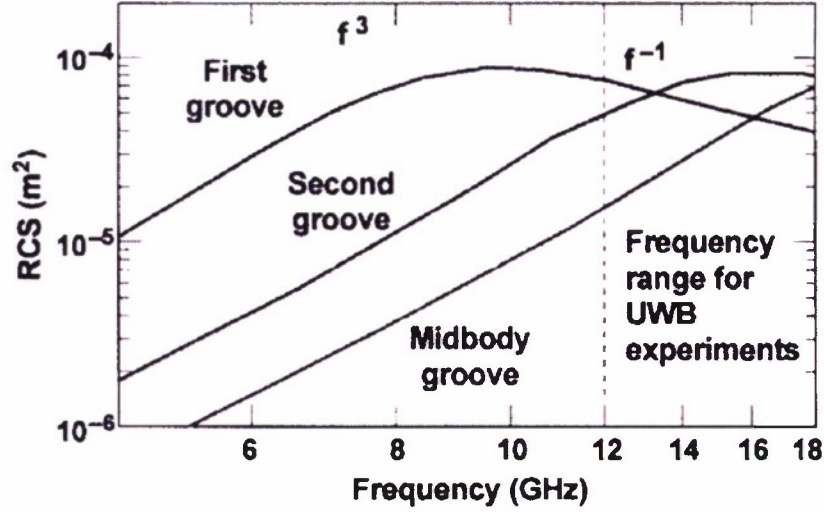


Figure 21. Groove frequency dependence

Another scattering mechanism appears in Fig. 22, which contains an example of how scatterers can sometimes be seen when out of classic visibility range. This is evident for the base edges being visible just beyond $\pm 7.2^\circ$ near 0.825 m, the cone's half angle. This is possible because travelling waves generated by scattering from the cone tip travel along the observed cone surface to diffract from the base corner and return via the same path.

We also see two traces in the figure between -50° and -30° and between 30° and 50° at a range of approximately 0.6 m at $\pm 45^\circ$. This trace appears at less than a base width past the range of the corners. Our preliminary analysis based on RCS computations of a simplified model indicate that the origin of this scattering is a surface current mode in the cone surface that results in a strong induced current source at the top and bottom of the base circumference. That is, these current maxima lie at $\pm 90^\circ$ with respect to the base-roll angle as compared to the usual HH polarization maxima at 0° and 180° . Because of its origin as a standing-wave phenomenon, this scattering mode is sensitive to the interrogating frequency and bandwidth, a behavior that is indeed observable in the various plots that follow.

Up to this point, the plots of scattering-feature range versus target-aspect angle only hinted at PSLI's super-energy resolution by using fading of each scatterer's color as an indication of its reflected energy. Fig. 23 aids in visually understanding each scatterer's range-energy- α relationship by showing how estimated parameters smoothly transition as aspect angle varies. Now there are four dimensions of information shown for target-feature identification: aspect angle, range, energy, and power law.

Fig. 24 illustrates PSLI's super-resolution in energy by plotting scattering energy versus aspect angle. The variation of energy level versus aspect angle is not a failure of the estimator but rather reflects the actual detailed scattering behavior of the complex target geometry (as is strongly

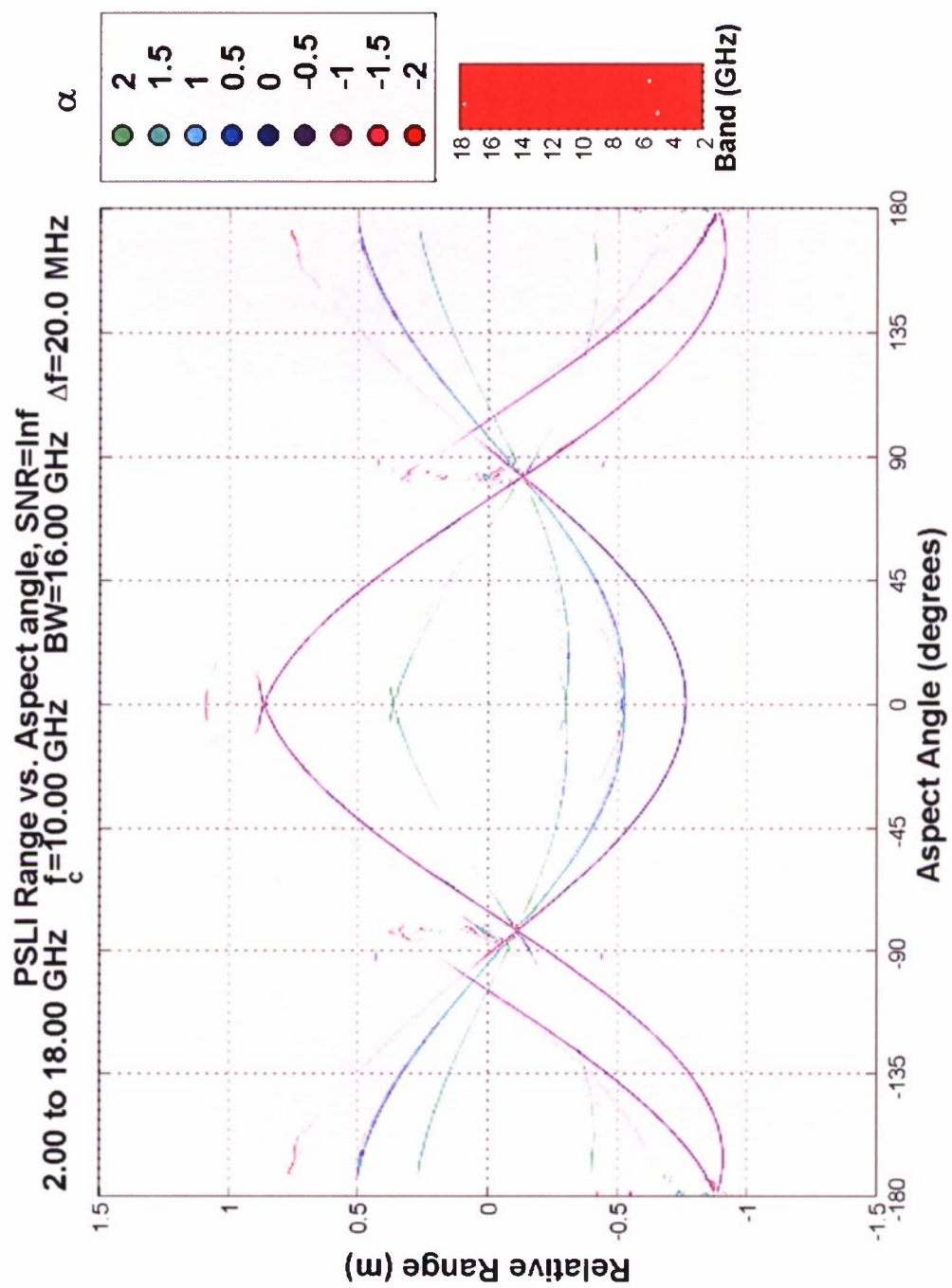


Figure 22. X-Band, 16.00 GHz bandwidth

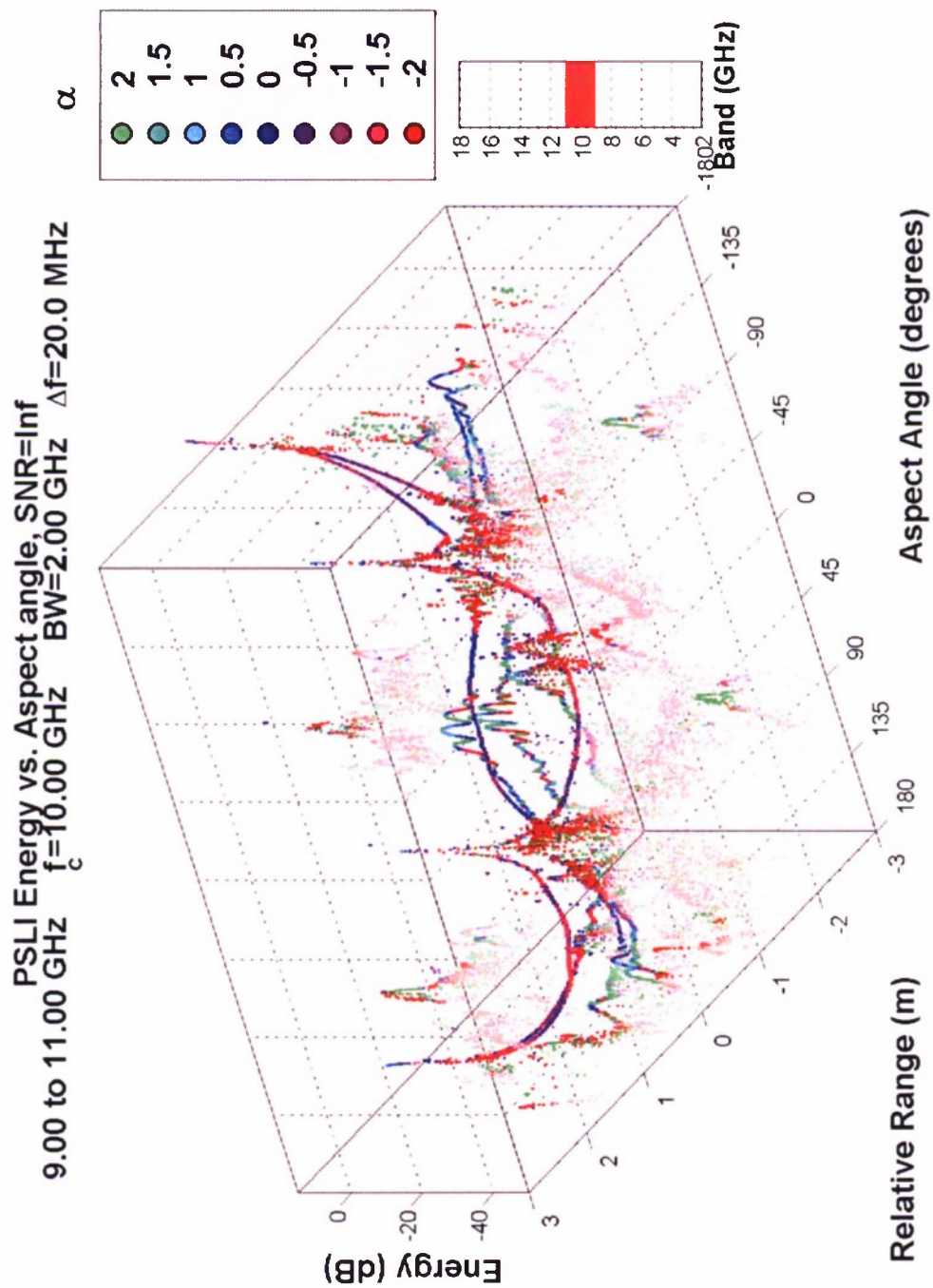


Figure 23. X-Band, 4.00 GHz bandwidth, 3D: Range & energy vs. aspect angle, and colored by power law.

indicated by the symmetry). Each of these peaks and troughs of the energy plot (and changes in α) are due to complex interaction of reflected waves travelling along the surfaces of the target. Thus the “spread” of Fourier tracks in traditional images that could easily be attributed to windowing effects are in many instances actually due to highly angularly dependent true variations in scattering amplitudes that can be recovered by PSLI for purposes of enhanced target recognition.

5.2 NARROWBAND ANALYSIS

Three bands were chosen due to their common use in radar applications for the plots presented in this section: S-, X-, and C-bands, centered at about 3 GHz, 5.5 GHz and 10 GHz, respectively. The descriptions for the S-band figures in this section hold true for both C and X-band, so we placed the C- and X-band plots in Appendix A. The purpose of this section is to show that even with small bandwidths, PSLI still obtains accurate α estimates.

Analysis of narrow bandwidth interrogations at S-band still present useful information for target recognition. Fig. 25 shows the target illuminated with only 250 MHz of bandwidth. One can see the resonances indicated by periodic fluctuations of α estimates occurring across the entire target azimuth range, but in particular, the aspect angles between $\pm 90^\circ$ through 180° show the frequency dependence oscillating between the extreme values of $\alpha = 2, -2$. Note that these resonances are symmetric about 0° indicating the target geometry based nature of these features. This is due to the symmetry of the target. These resonances were not seen at larger bandwidths, because every frequency component gives rise to its own resonance distribution. A large bandwidth solution effectively averages over these many oscillating traces resulting in a single smooth curve about the average energy return and position associated with the ensemble of traces. The cone tip, found at range -0.765 m, has a distinctive and strong pattern between $\pm 45^\circ$. It begins as an α of 2 at 0° , stays constant until about 20° , then oscillates between plus and minus 2. The base edges show similar effects, although between $\pm 30^\circ$ and 60° , the transition passes through all values of α as opposed to switching directly from plus to minus 2.

Using a bandwidth that is twice as large, 500 MHz in Fig. 26, the resonances still occur, but with the added feature of resolving both base edges for additional aspect angles. The double diffraction at 0° and 0.95 to 1.15 m, above the base edges, seen before in the ultra-wide bandwidths above is once again visible. Note that the double diffraction also experiences the same resonances that affect the base edges.

In this same figure, the first and third grooves are not visible, although the second groove is oscillating in range and α as seen between azimuth angles $\pm 30^\circ$, over the range ± 0.2 m centered about -0.35 m. Again, this is a result of interrogation at this particular bandwidth which exposes the standing waves associated with the geometry of the cone at this excitation frequency. For aspect angles $> |100|^\circ$, even though the cone tip is shadowed, it still has a ghost trace in its place.

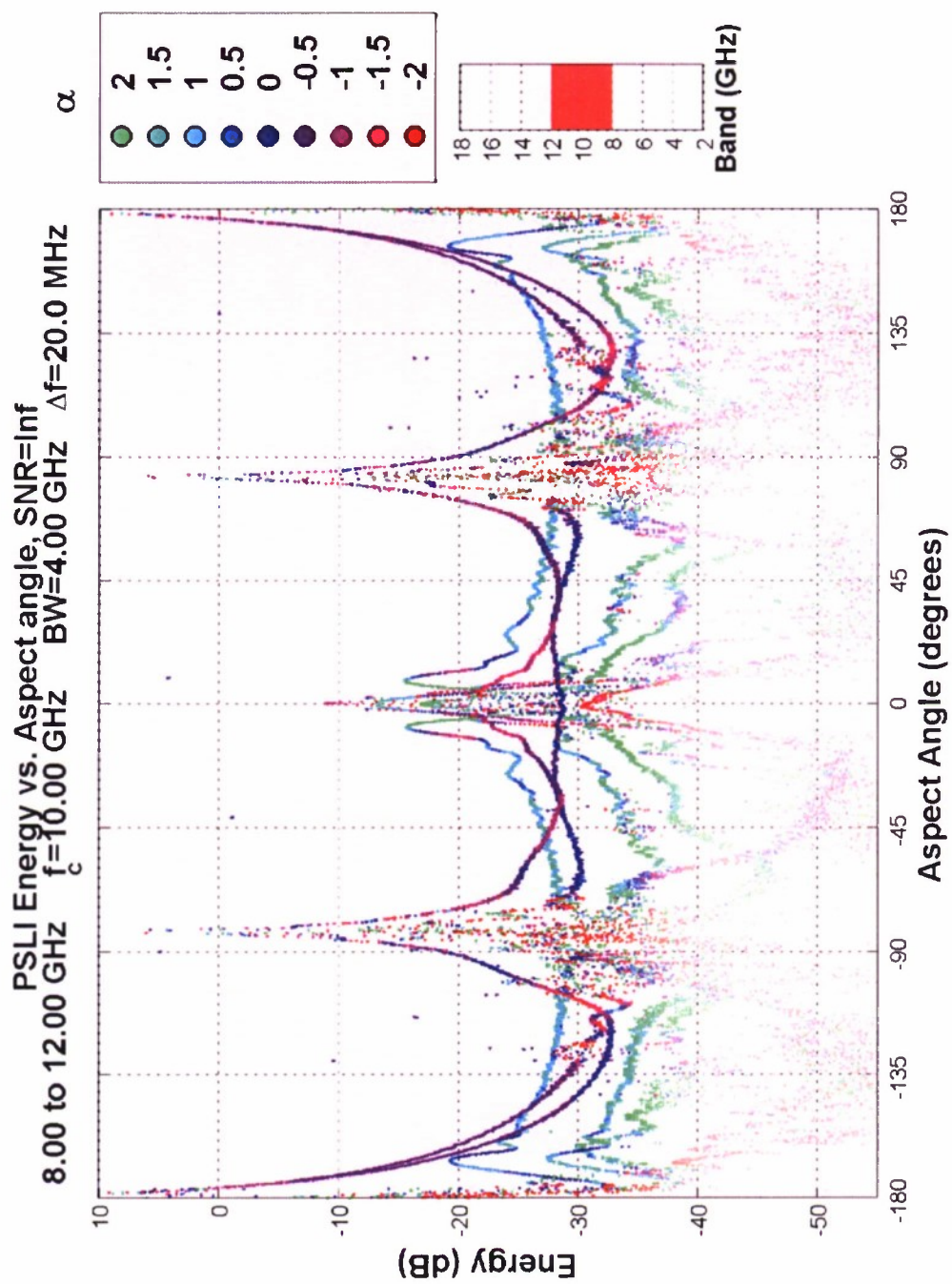


Figure 24. X-Band, BW=4.00 GHz, Energy versus aspect angle.

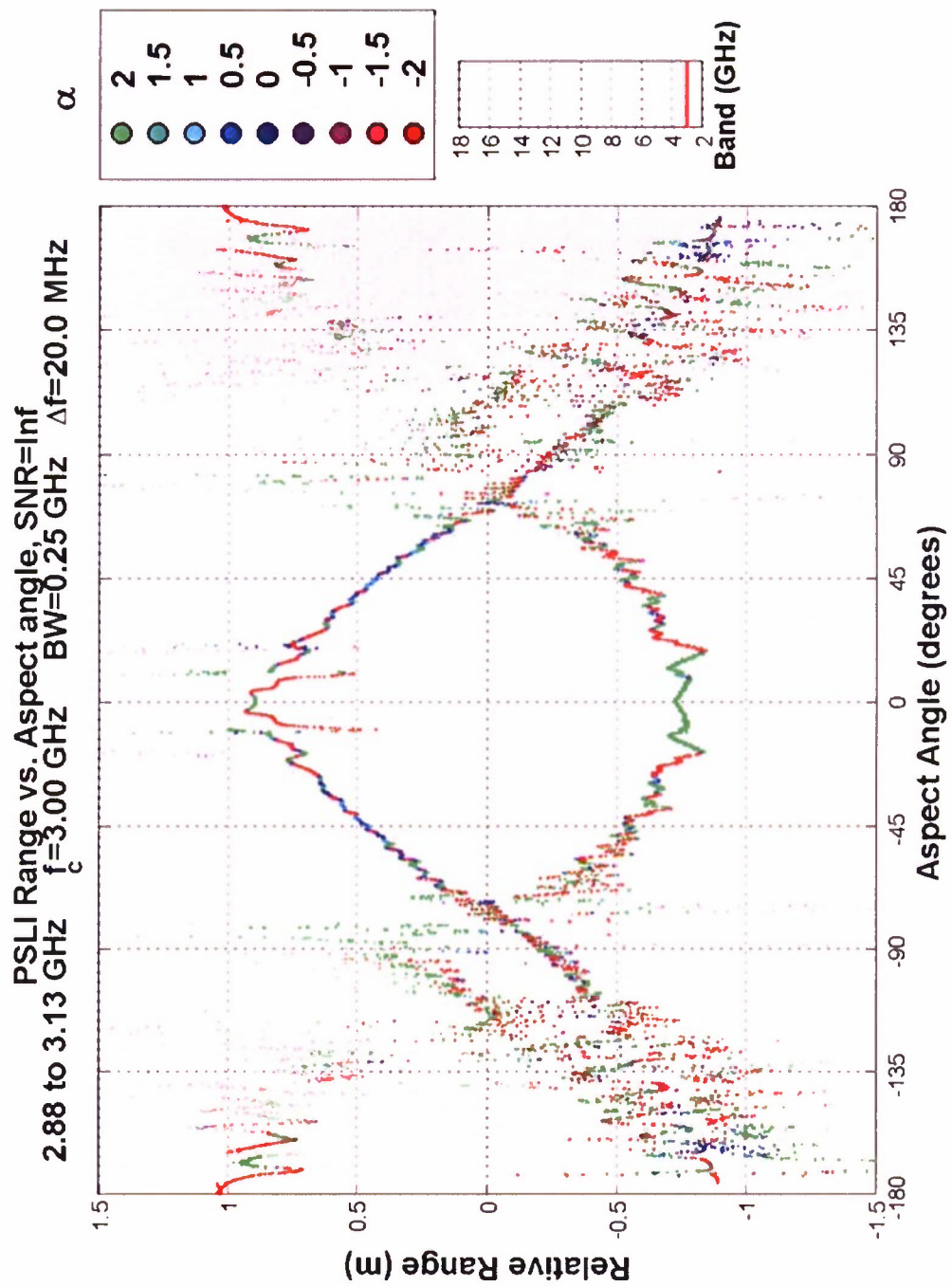


Figure 25. S-Band, 0.25 GHz bandwidth

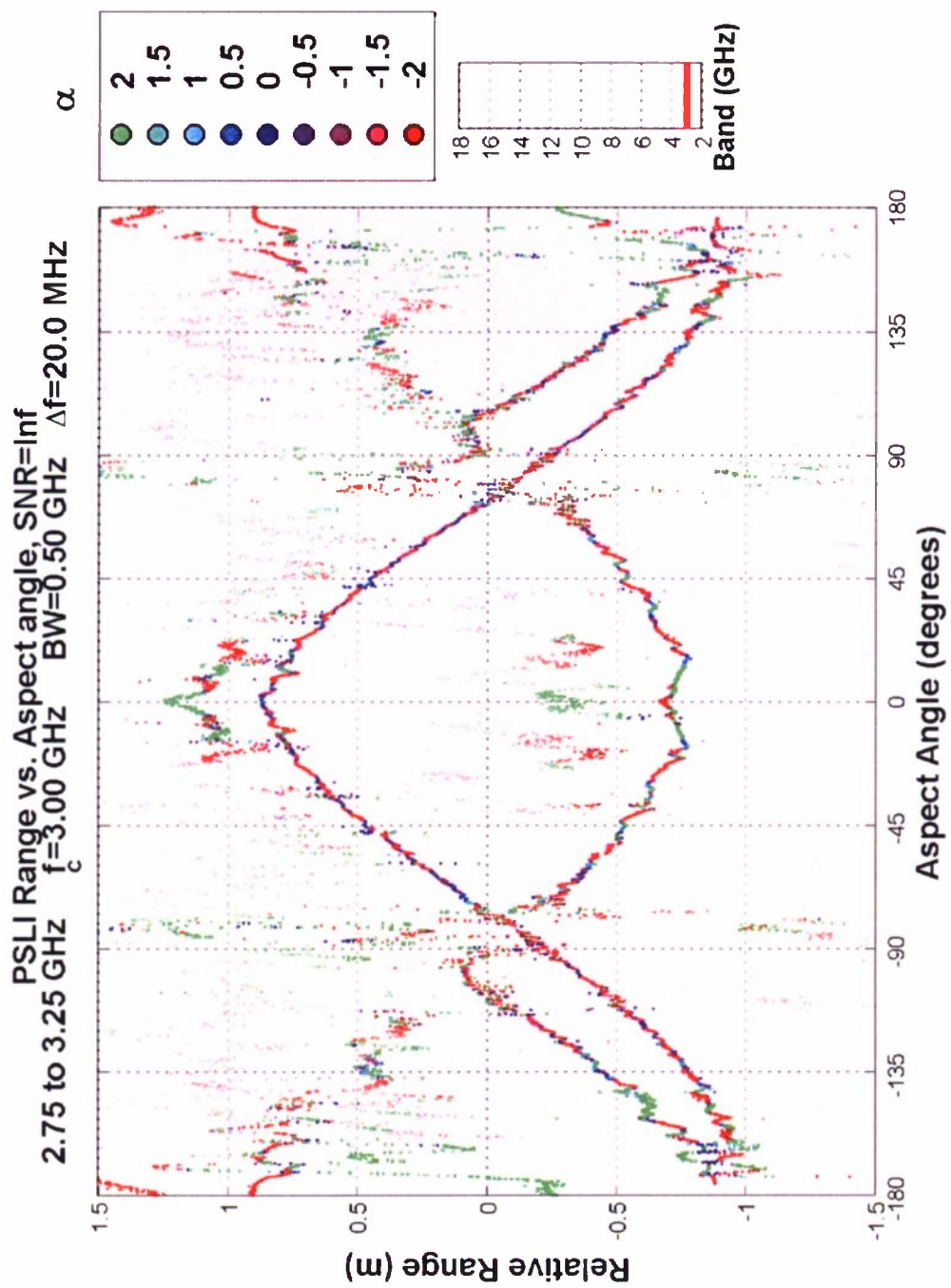


Figure 26. S-Band, 0.50 GHz bandwidth

As shown in the previous section, PSLI provides super-resolution in energy, as well as range. Fig. 27 shows an example of this for S-band with 500 MHz of bandwidth. Note that the resonances which appear in the range view, also appear strongly in the energy view. As each scatterer's power law transitions from one to another, the energy level similarly changes. This is shown on the energy curve found at -30 dB near azimuth angle -45° .

A zoomed-in look at the nose tip may be seen in Fig. 28. The resonances change roughly every 10° with a distinctive and symmetric pattern about the 0° azimuth.

Much of the detail found in the wideband figures is seen to some extent in Fig. 29. Both the first and third grooves are now visible, along with the low returns from the shadowed base edges. The change in range estimates due to resonances is much more subdued in the figure. As explained above, this is due to having wider bandwidth. The base double diffraction appears strongly in this figure. Instead of being restricted to $\pm 10^\circ$ and near -1.1 m, it now appears to extend at a lower energy outward until it meets with the furthest base curves near 0 m.

Fig. 30 shows the noteworthy performance of the 500 MHz bandwidth analysis with a low SNR of 15 dB. Of course the features which were below this SNR threshold are not detected, but the strong base edges clearly shine through the noise. The familiar resonances may be seen at the outer edges of the figure from $\pm 135^\circ$ to 180° . They change rapidly from plus 2 to minus 2 without passing through an α of 0. The α of minus 2 is prominent near $\pm 75^\circ$ as well as near 0° .

5.3 PSLI COMPARISON WITH FOURIER AND NEM

This section presents comparisons of PSLI with both Fourier and NEM processing methods. We will first discuss PSLI's advantage over Fourier processing and then cover the differences between PSLI and NEM.

Fig. 31 illustrates PSLI's superior ability to resolve individual scattering centers as compared to Fourier processing for S-band with a 25 dB SNR. Similar plots for C- (Fig. A-6) and X-bands (Fig. A-12) may be found in Appendix A. Note that unlike previous target-range plots, these three figures use color to indicate scatterer reflected *energy* and not power law, because Fourier processing does not identify frequency-dependent scattering information.

In the PSLI vs. Fourier figures, PSLI resolves scattering centers with greater precision than the blurred Fourier images even with a data set having 25 dB SNR. The blurring of Fourier images is due to *spectral leakage* of scatterer energy across range gates [23]. Super-resolution techniques such as PSLI can super-resolve scattered energy levels as well as range. Here, it is noteworthy that the PSLI method determines the *true* energy reflected by each scatterer and not *pseudo* energy which many super-resolution techniques yield.

If we were to forgive Fourier processing for its lack of power-law identification and super-resolution, it appears the only benefit that Fourier processing has over PSLI is speed. Table 2 presents execution speeds (measured in average pulse repetition frequency, PRF) for Fourier, PSLI, and NEM processing bandwidths from 0.5 GHz to 8 GHz attained with a commercial numerical package, MATLAB, on a workstation. Here we find that at 0.5 GHz bandwidth with 25 frequency

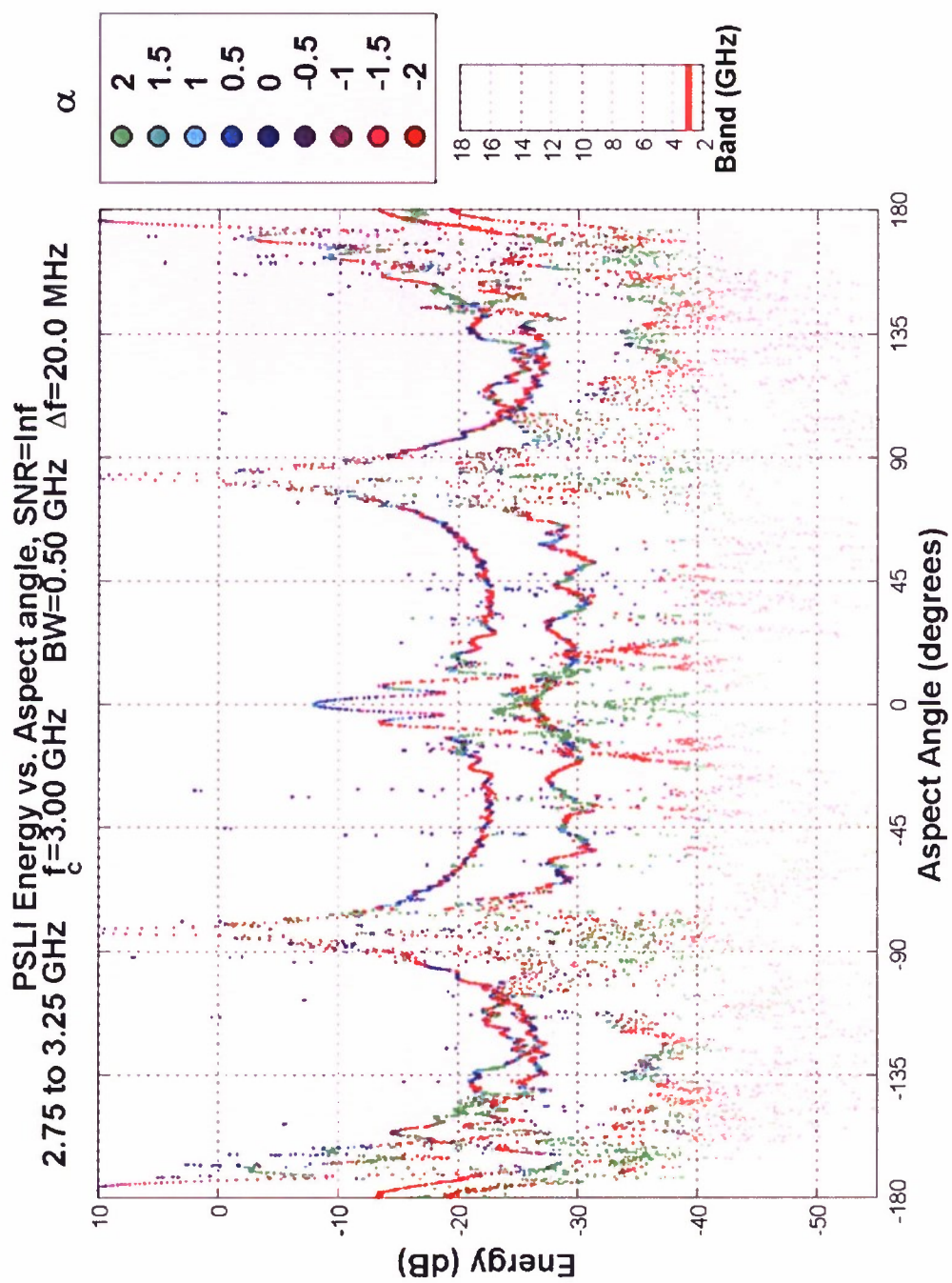


Figure 27. S-Band, 0.50 GHz bandwidth, Energy

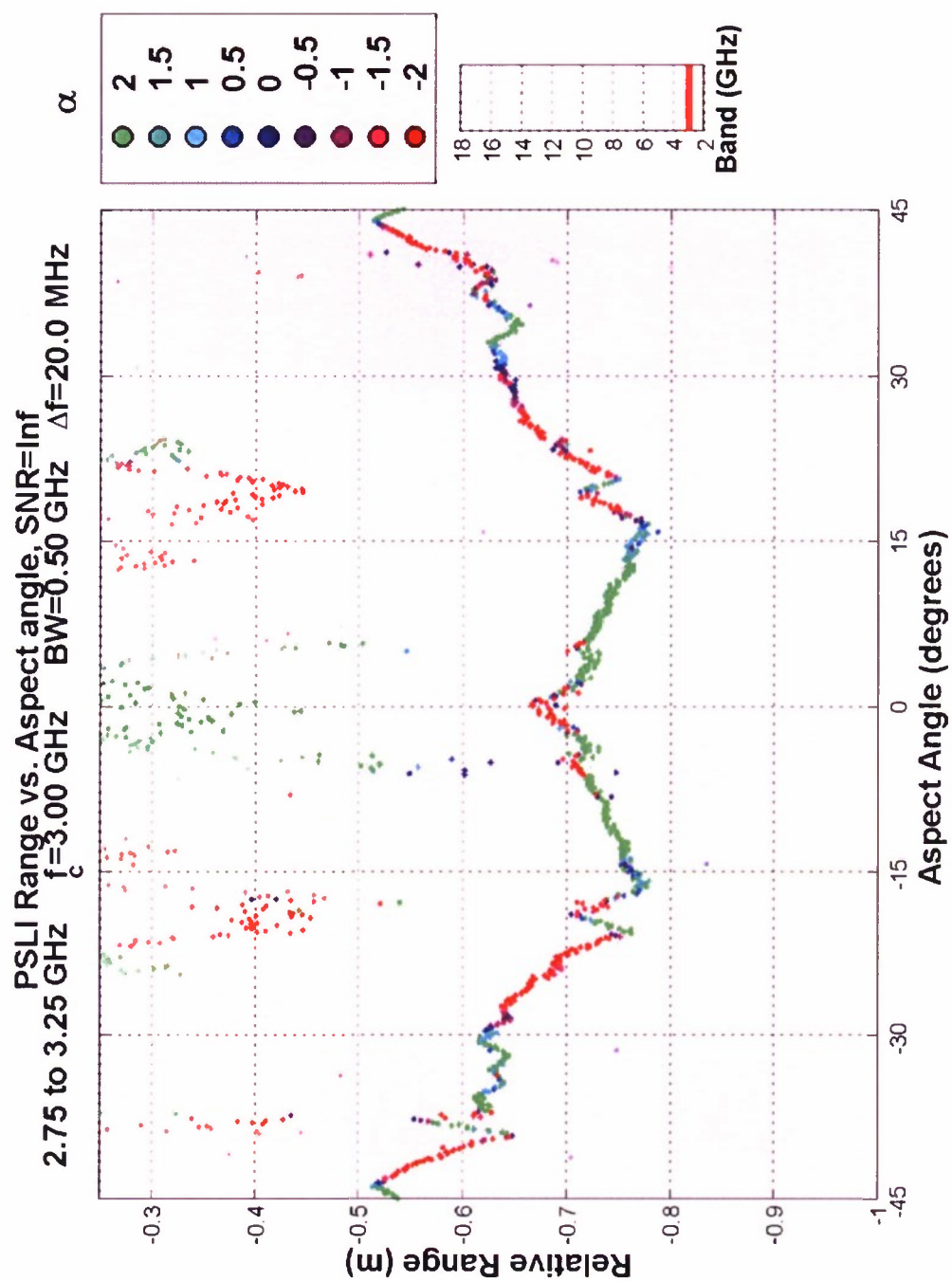


Figure 28. S-Band, 0.50 GHz bandwidth, zoomed on the cone tip.

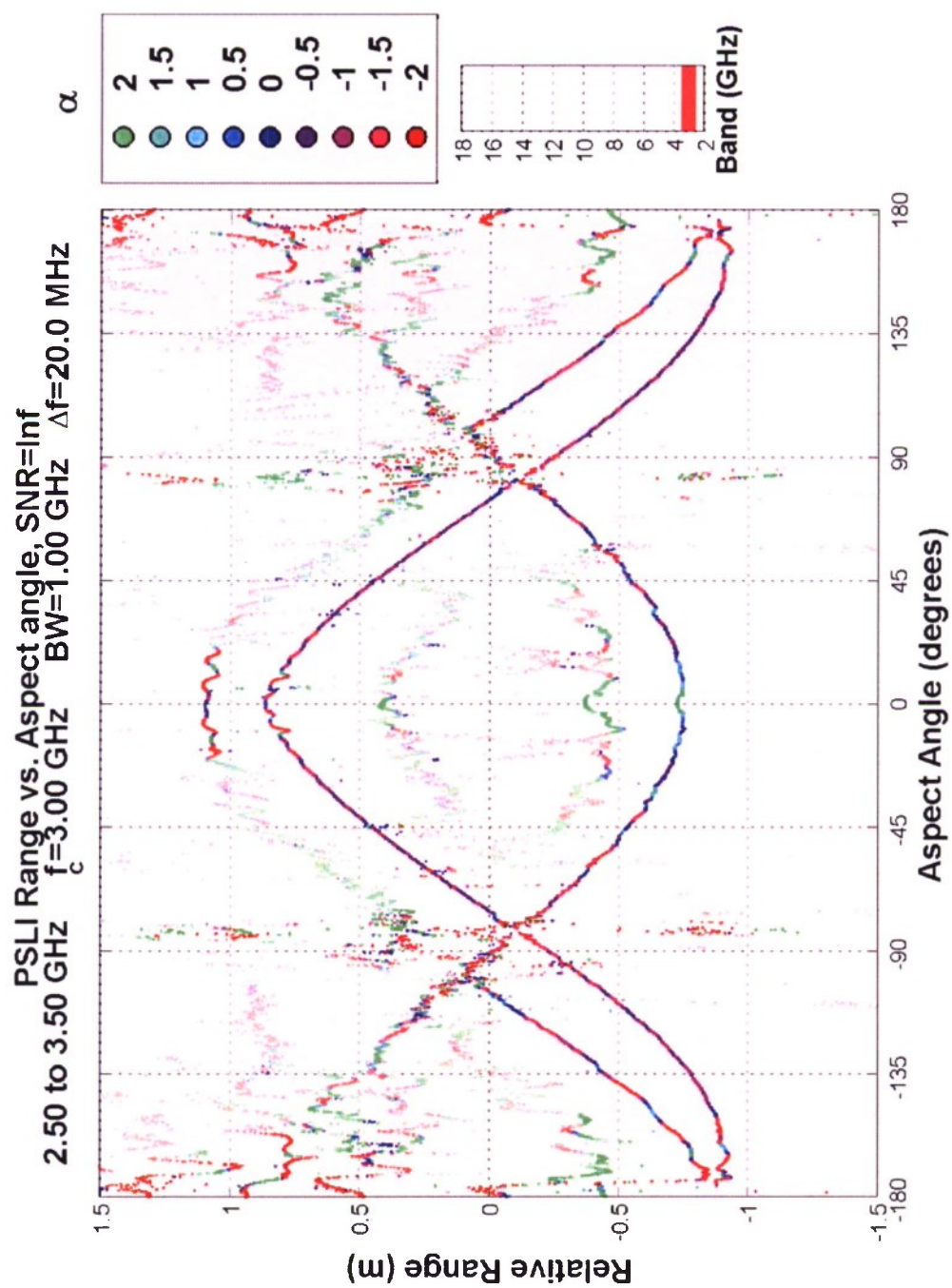


Figure 29. S-Band, 1.00 GHz bandwidth

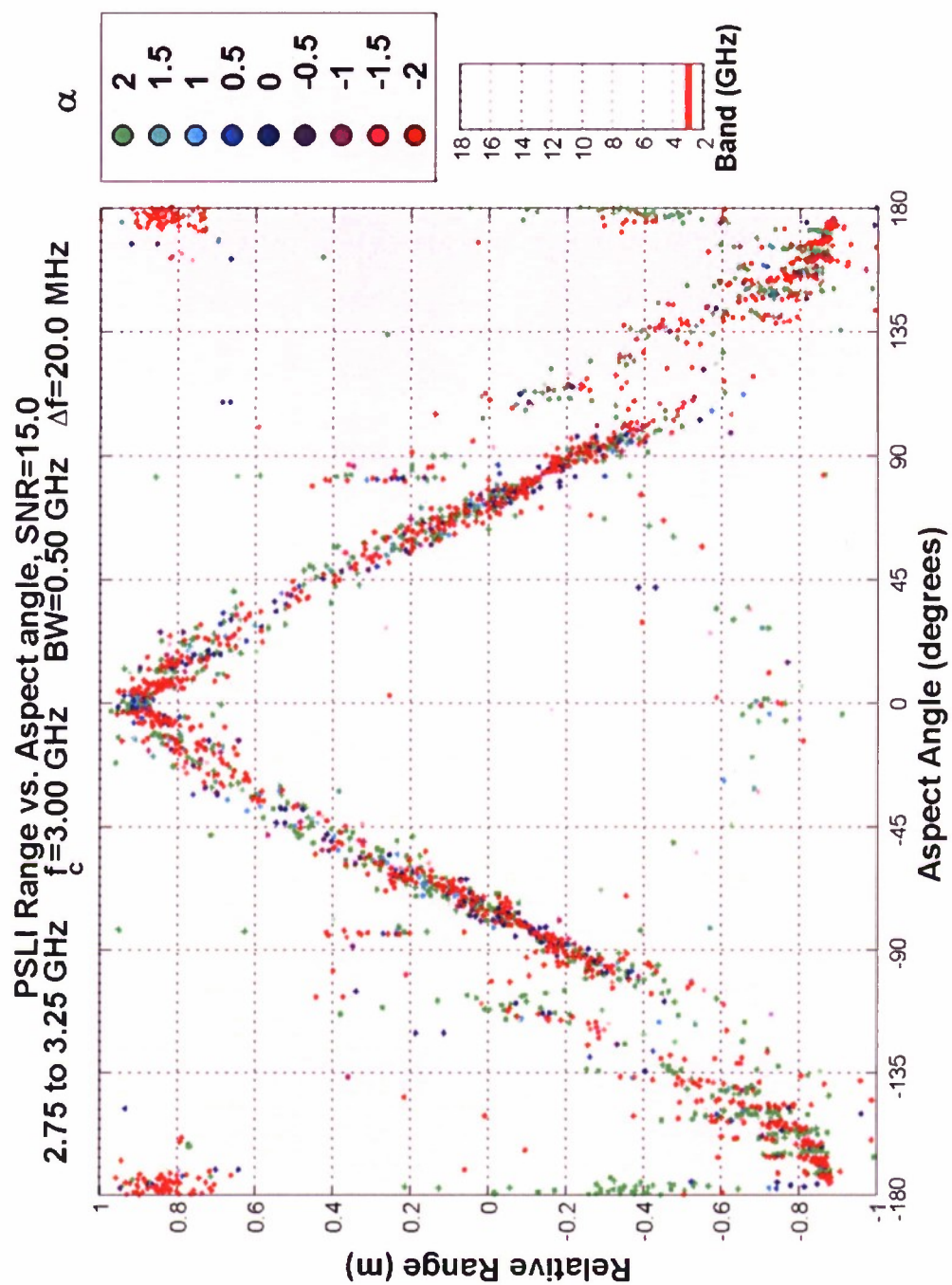


Figure 30. S-Band, 0.50 GHz bandwidth and 15 dB SNR

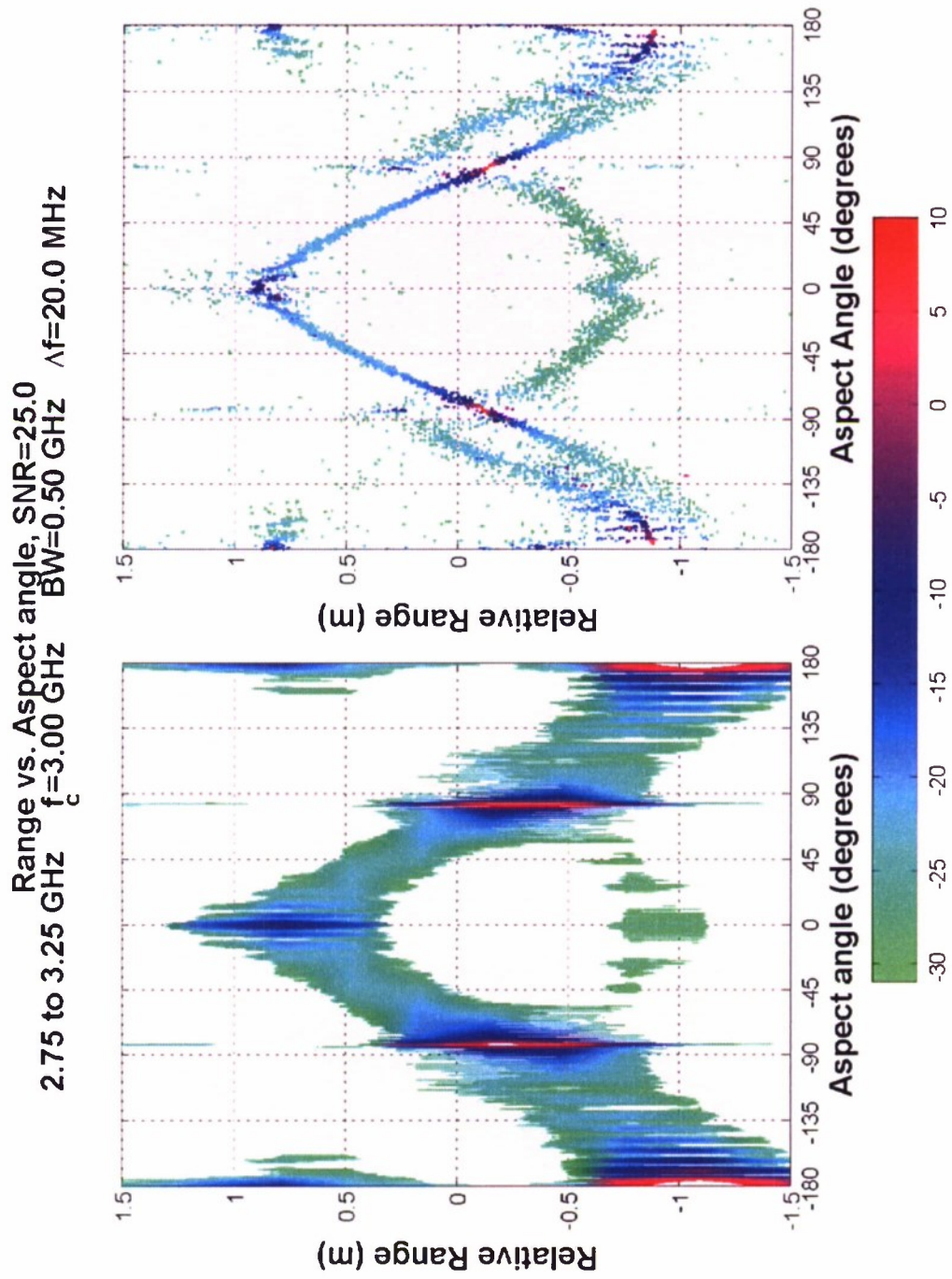


Figure 31. Fourier vs. PSLI, S-Band, 1.00 GHz bandwidth, 25 dB SNR

samples per interrogation, MATLAB's FFT⁴ function attains a PRF of 8.24 kHz while PSLI reaches 234 Hz, about 35 times faster. At 8 GHz bandwidth with 401 frequency samples, MATLAB's FFT is about 865 times faster. This is because the FFTW implementation has a worst case computational growth of $N \log N$, while PSLI grows roughly as N^3 as explored in Section 3.5.4.

TABLE 2
Speed Comparison using MATLAB 6.5 on a 3 GHz Intel Pentium 4 running
Microsoft Windows XP, assuming 8 scatterers for Fourier processing, PSLI,
and NEM.

Interrogation Data		FFTW (PRF) Total	PSLI (PRF)			NEM (PRF)		
Bandwidth (GHz)	# Freq. Samples		Range	α	Total	Range	α	Total
0.50	25	8240	950	310	234	470	4	4
1.00	51	7200	550	200	147	230	3	3
2.00	101	5625	180	75	53	70	1.5	1.5
4.00	201	3490	35	15	10.5	15	0.9	0.8
8.00	401	1557	4.1	3.2	1.8	1.6	0.3	0.3

However, if we want to identify an individual scatterer's power-law frequency dependence, then Fourier processing is not an option, and we must compare PSLI with NEM. From Table 2, we find that when processing 0.5 GHz bandwidth interrogations (25 samples), PSLI achieves a PRF that is about 58 times faster than NEM's 4 Hz PRF. At 4 GHz bandwidth, PSLI achieves rates 12 times greater than NEM and, at 8 GHz bandwidth, PSLI is only 7 times faster than NEM.

At first it appears that PSLI is losing its speed advantage at higher bandwidths, but recall from Chapter 4 that NEM fails for large bandwidths. Comparing PSLI with NEM at 2 GHz bandwidth, frequency range of 2 GHz to 4 GHz in Figures 32 and 33, we note that both processing algorithms perform similarly for scattering-feature range and power-law identification. However, when processing 9 GHz bandwidth data (frequency range of 2 GHz to 11 GHz) as can be seen in Fig. 34, the NEM algorithm breaks down for this ultra-wideband processing while PSLI continues to perform correctly. In the NEM generated plot, scatterers are completely missing in angular segments such as between $\pm 5^\circ$ and 30° due to lack of Newton-Raphson iteration convergence.

To summarize, although Fourier processing was faster than PSLI and NEM, it suffers from spectral leakage and thus does not provide super-resolution in range or energy estimates. Furthermore, FFT processing does not extract any frequency-dependent scattering information. Comparing PSLI with NEM, we found that PSLI is faster, and, due to the PSLI algorithm's direct solution technique, PSLI does not suffer from convergence failures for large bandwidth data.

⁴As of MATLAB 6.5, its discrete Fourier transform command, FFT, uses a package called the "FFTW: Fastest Fourier Transform in the West" (available from MIT for commercial licensing).

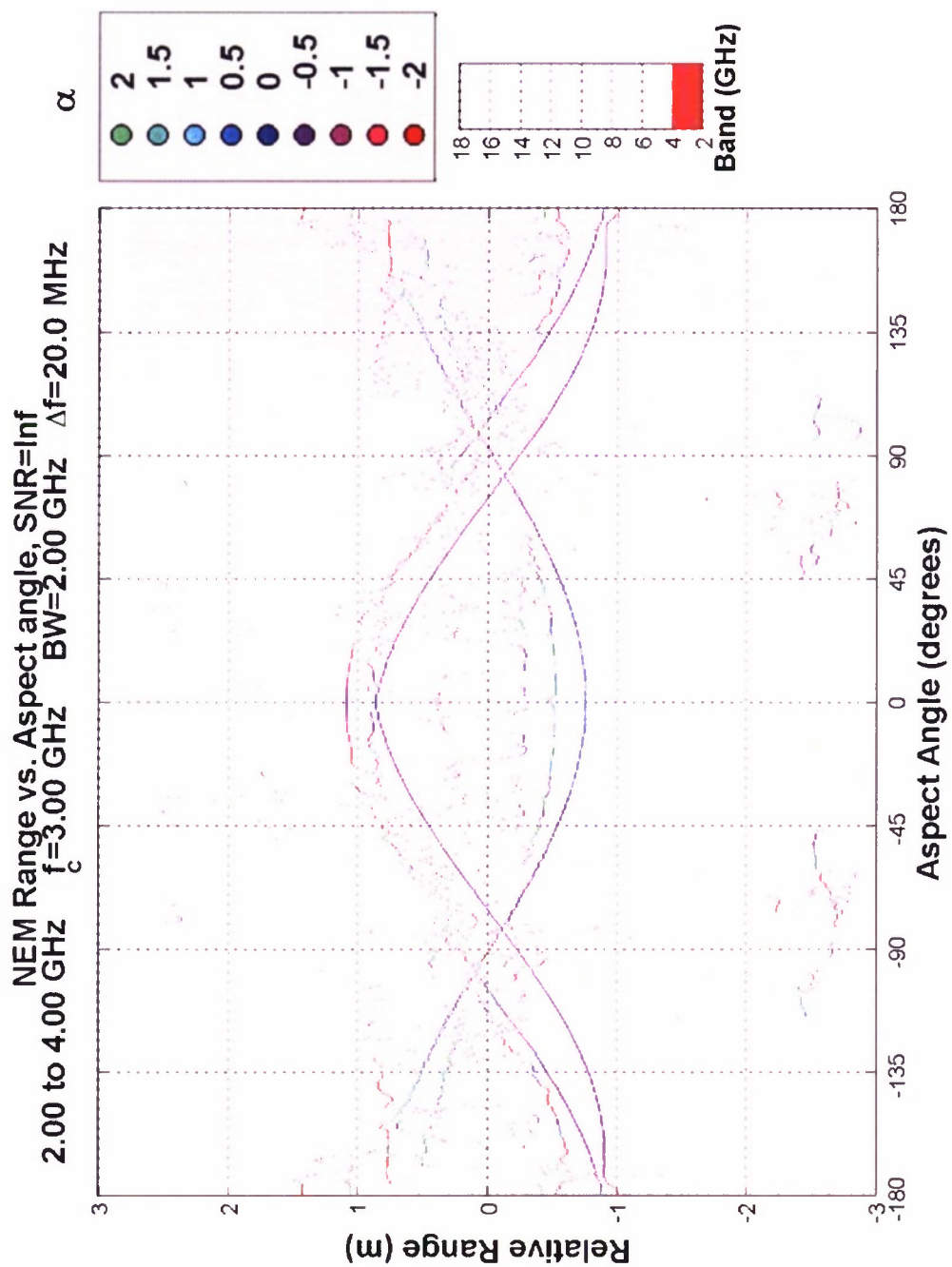


Figure 32. NEM, S-Band, 2.00 GHz bandwidth

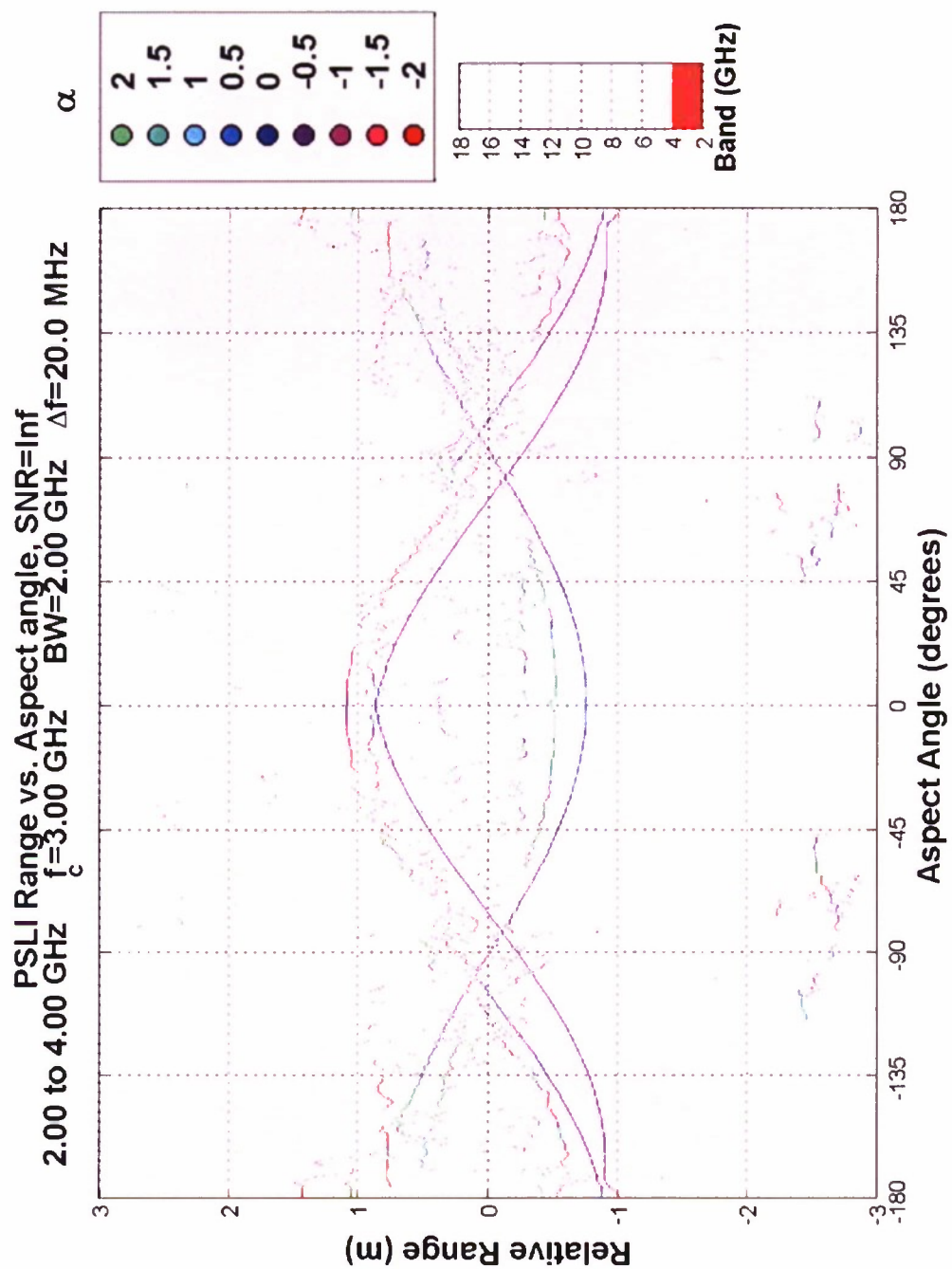


Figure 33. PSLI, S-Band, 2.00 GHz bandwidth

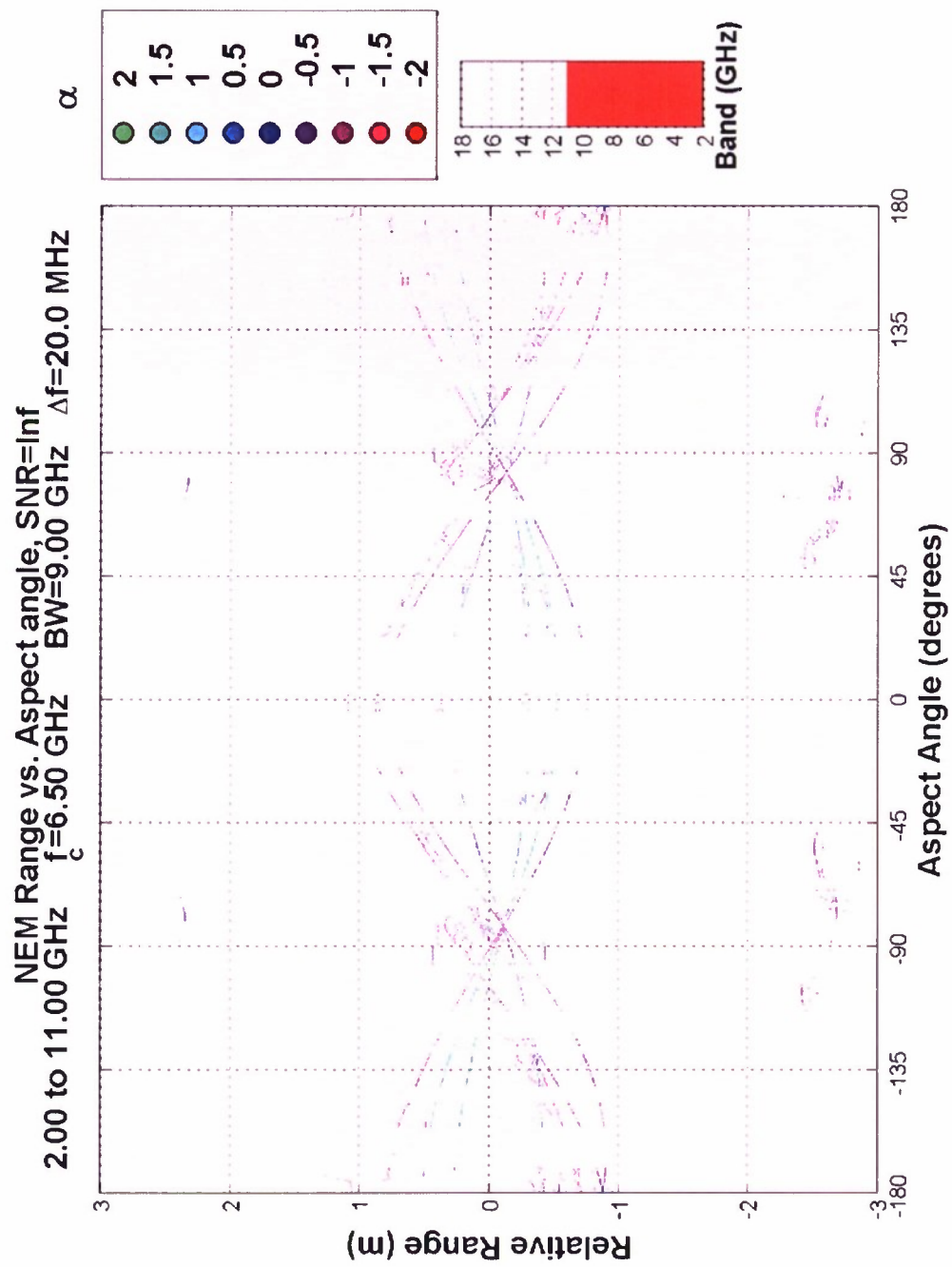


Figure 34. NEM 6.50 GHz center frequency, 9.00 GHz bandwidth

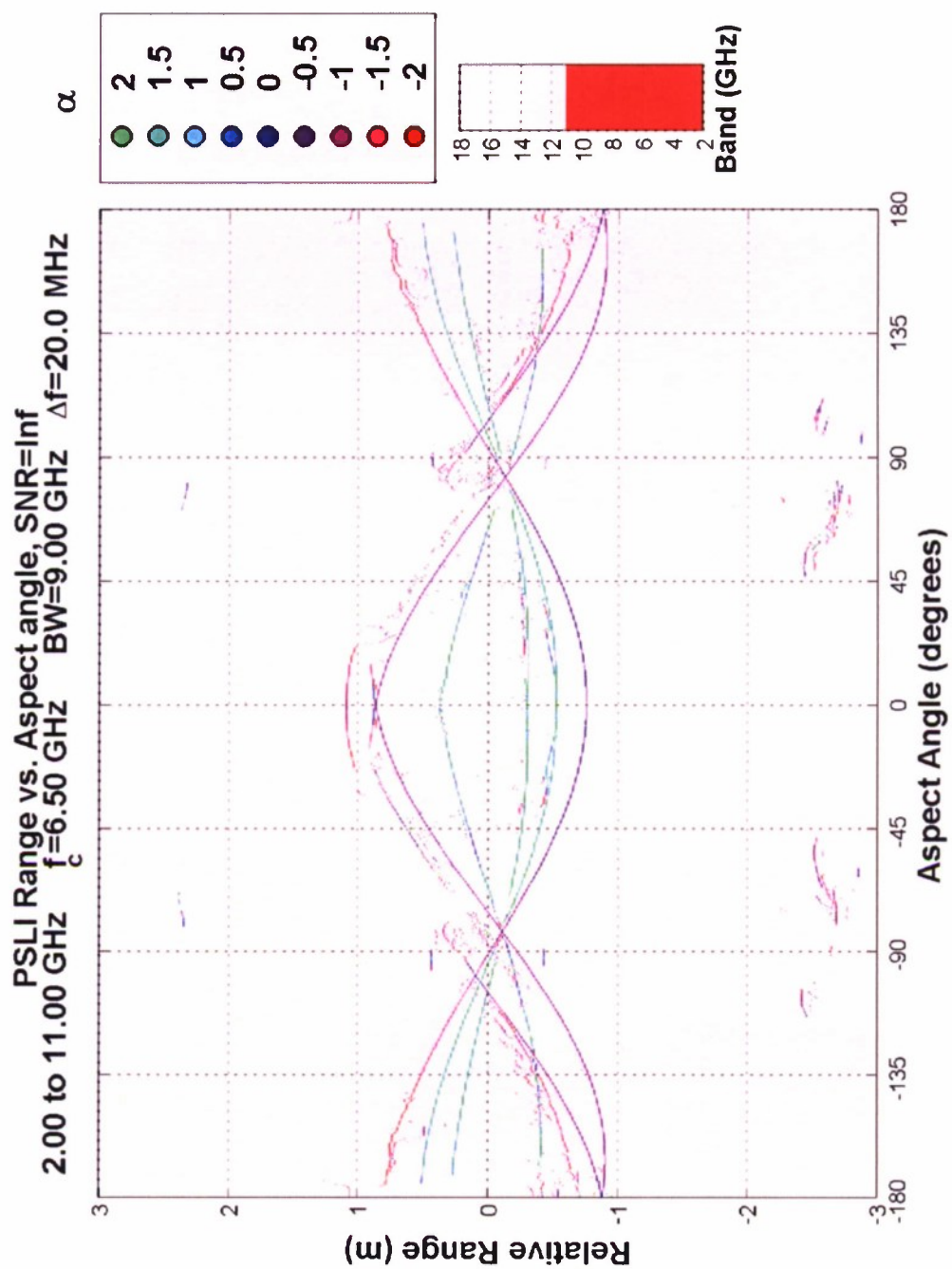


Figure 35. PSLI 6.50 GHz center frequency, 9.00 GHz bandwidth

6. CONCLUSIONS

In this project we have developed a new modern spectral-estimation algorithm, PSLI, for the enhanced super-resolution radar analysis of frequency-dependent scatterers employing a signal model based on the geometric theory of diffraction. The novelty of the approach can be summarized as follows:

- It directly treats the problem of extracting positive-integer exponent, power-law dependent, scattering-center locations and amplitudes by exploiting a new approach for finding eigenvalues with multiplicity associated with idealized signal models despite matrix perturbation due to noise.
 - A Schur-decomposition-based approach is introduced that avoids the numerical ill-conditioning associated with extraction of eigenvalues with multiplicity which cause instability of some estimators and/or require the inclusion of dithering noise sources to induce stability.
 - The approach is noniterative in form and hence gives rise to radar estimation with fixed execution time—this is an important feature in the system engineering of real-time systems.
 - Because it addresses the problem of power law models directly, it is not subject to breakdown for narrow or wide bandwidth data. In this sense it anticipates the needs of future ultra-wideband radar system.
- The overcomplete nature of the full GTD scatterer-model basis (positive and negative half-integer power laws) is recognized. We introduce the vector-channel method, well known from communication theory, to obtain GTD models from the positive integer models that yield to a numerically well-conditioned solution.
- The positive-integer power law (PIPL) decomposition introduced in PSLI directly provides a Taylor-series model for the frequency dependence of scatterers that does not reduce the description of a feature's characteristic frequency behavior to a single dimension as does the GTD model and exponential models. Thus it opens the possibility for vector-attribute-based feature processing for target recognition that offers the potential for significant improvement in target identification performance.
- Means were also implemented to further process the data with respect to the identified GTD-model half-integer scatterers from the vector-channel decision system to obtain the true scattered energy from each such scatterer (in contrast to the pseudo-spectral values associated with some super-resolution techniques.)

Thus in summary, PSLI is suited as a direct replacement for Fourier transforms in radar imaging applications. This work suggests the need to further investigate the possibility of exploiting full PIPL-basis attribute vectors rather than less general GTD basis for enhanced ATR applications.

In Chapter 4, we compared the theoretical performance of PSLI with the Cramer-Rao bound and with that of the Nearest Exponential Model, NEM, approach for identifying the power law for a single, synthetic scatterer. With respect to the Cramer-Rao bound on parameter estimation variance, PSLI produces high-quality estimates of scatterer frequency-dependent power laws from narrow to ultra-wide bandwidths while NEM fails at large bandwidths due to the failure of the exponential model it incorporates to properly represent power-law behavior over large bandwidth intervals.

Chapter 5 continued the evaluation of PSLI using a static-range data set obtained for the LL-Cone target. We showed that for S-, C-, and X-bands, PSLI provides accurate and enlightening power-law estimates for narrow and wide bandwidths. It was shown that power-law parameter values predicted by GTD for certain major target features were indeed correctly estimated by PSLI. We then demonstrated the power of PSLI to find more complex scattering mechanisms and assist in the identification of those mechanisms through its identification of power-law parameters.

It was also demonstrated how power-law values can become obscured by sufficiently large bandwidths when the power-law dependence is itself frequency dependent. The Taylor-series scheme for power-law attribution described above can become a powerful tool in the future for complete characterization of features that undergo resonance or other induced changes in behavior over the frequency range of the observation bandwidth.

The PSLI results also help identify the global-object geometry information that is to be found in azimuth-angle dependence of the power-law parameter. These variations come about from changes in the phase relationships between standing wave modes on the surface of the target with respect to the radar aperture as a function of azimuth.

Of special note is this work also revealed the notion that at low bandwidths, the oscillations in GTD power-law parameter values, scattered-energy values, and range values are not due to estimation failures, but rather are an integral feature of scattering behavior and potentially are another valuable feature attribute for target identification.

Finally, in this chapter we found PSLI to be faster, as seen in Table 2, than NEM, and we again demonstrated that the NEM algorithm has difficulty processing ultra-wide bandwidth data. Finally we demonstrated, in comparison to Fourier-based processing, PSLI provided super-resolution in range *and* in energy while retaining super-resolution of features even in low SNR environments. We argue that the variation in scattering-center positions versus azimuth angle for narrow bandwidth pulses is not a breakdown of super-resolution methods such as PSLI but is actually a true measure of the scattering currents in target surfaces and their phase relationships with respect to the driving field. By better understanding these RCS phenomena and incorporating them into future imaging systems one might hope to someday create a next generation of super-resolution imaging systems that effectively pinpoint physical features despite these phenomena.

APPENDIX A

ADDITIONAL STATIC RANGE RESULTS

The figures in this appendix are similar to those found previously in the report, but at differing center frequencies. The descriptions for the the C- and X-band figures are the same as found for their S-band counterpart. The caption below each figure states where this similar S-band description may be found in the report.

A.1 C-BAND

This section contains various figures with center frequencies of 5.5 GHz.

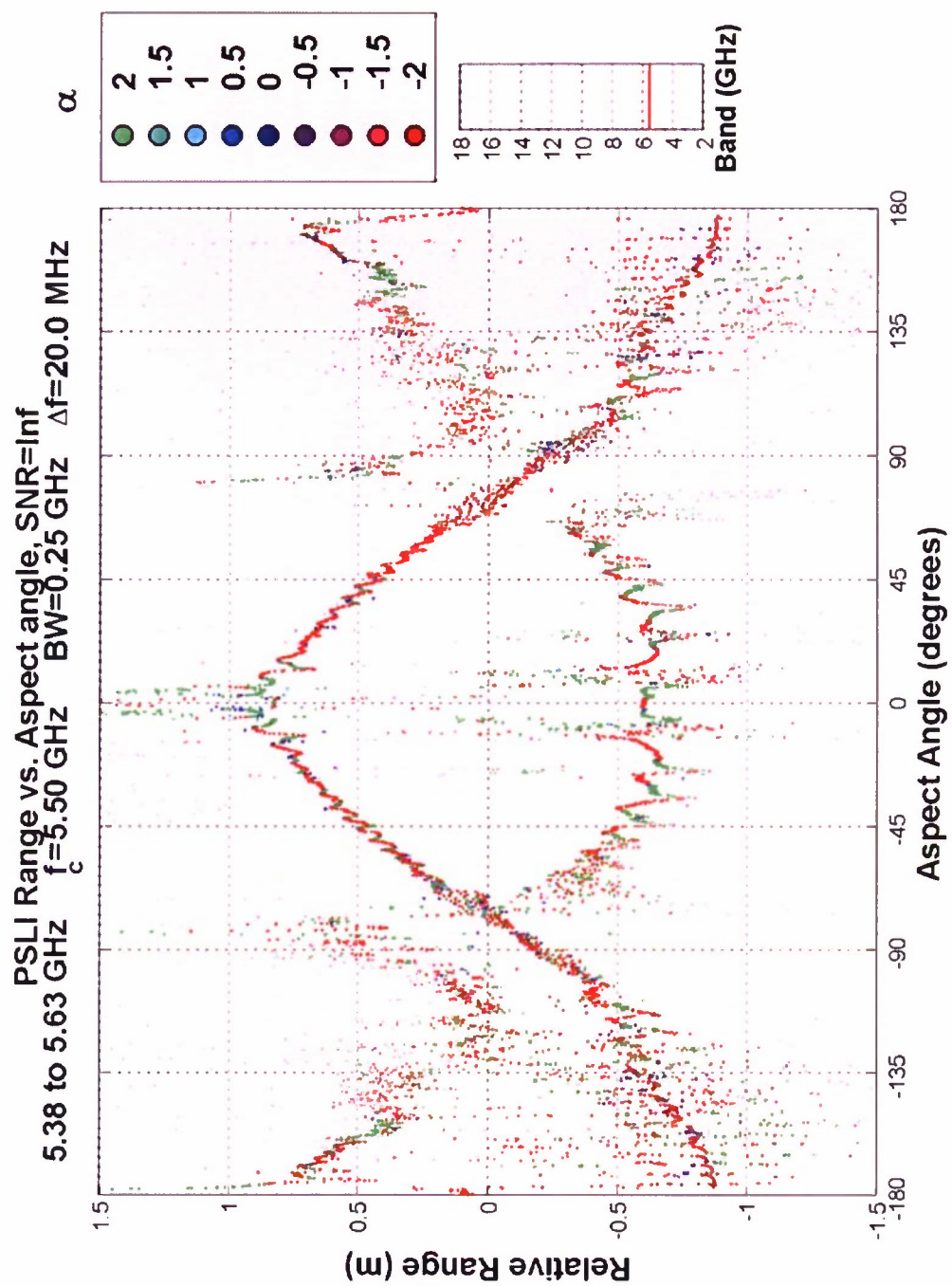


Figure A-1. C-Band, 0.25 GHz bandwidth, Description found with Fig. 25 on page 36 in Section 5.3

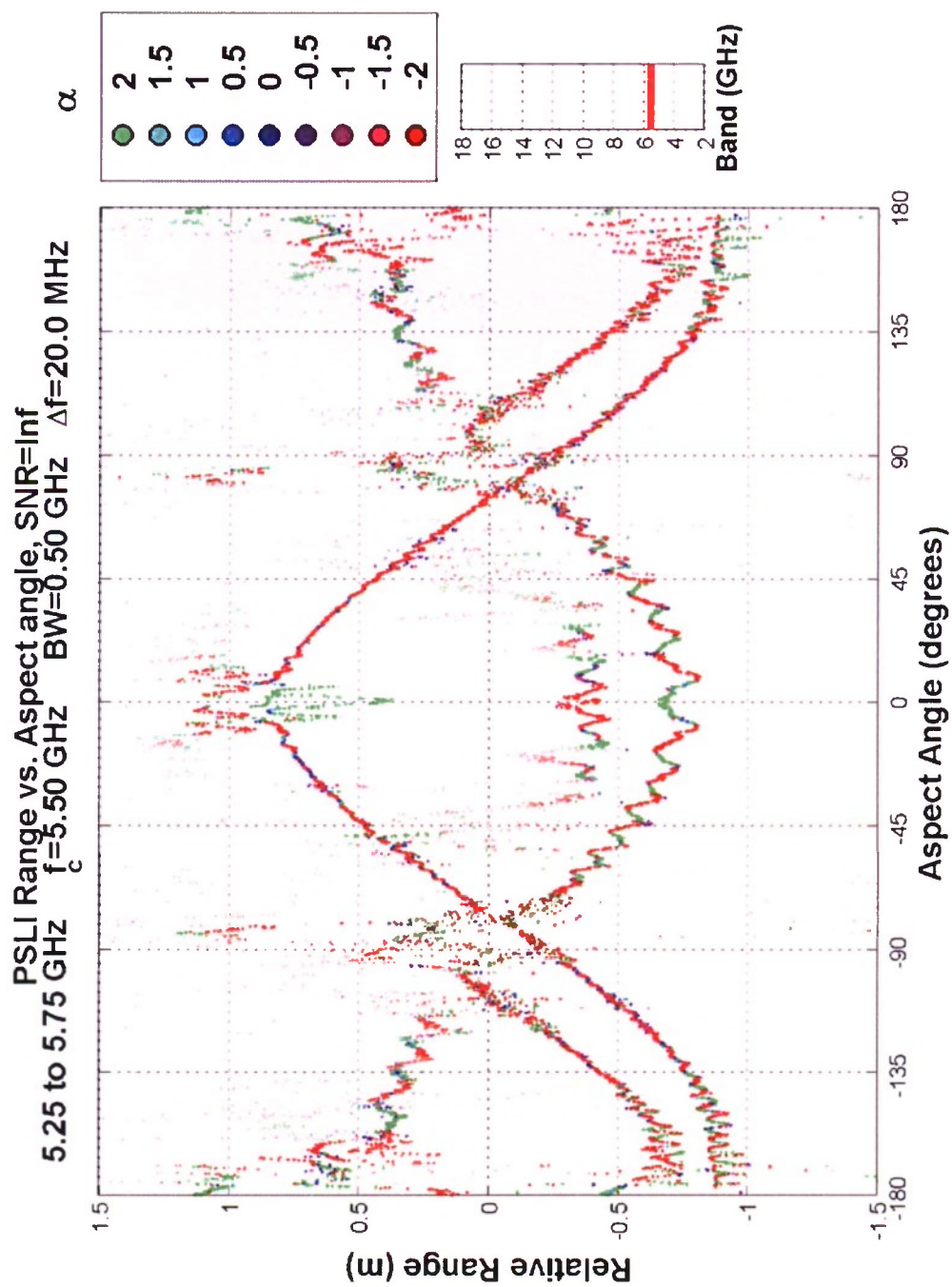


Figure A-2. C-Band, 0.50 GHz bandwidth, Description found with Fig. 26 on page 36 in Section 5.3

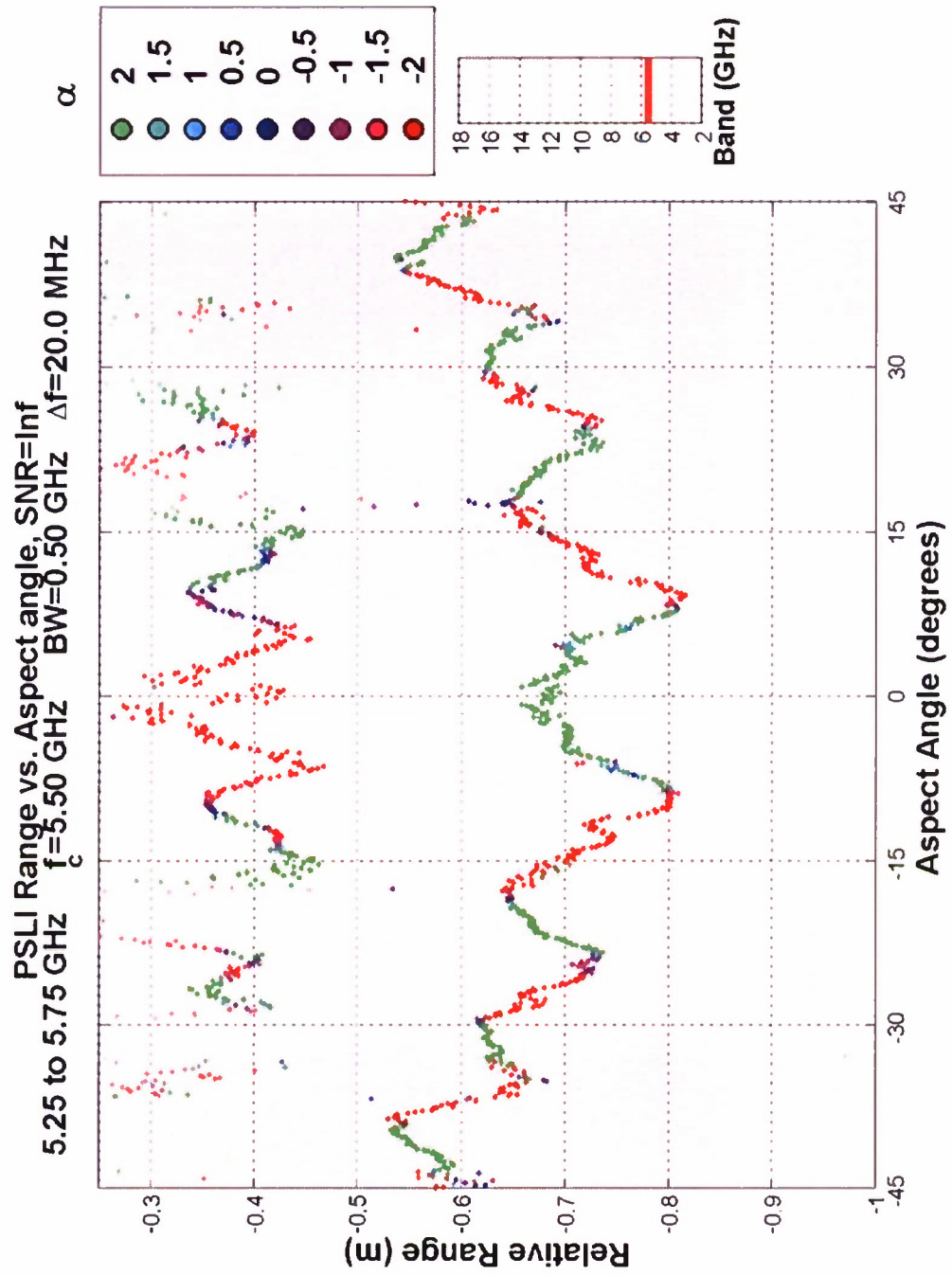


Figure A-3. C-Band, 0.50 GHz bandwidth, zoomed on the cone tip., Description found with Fig. 28 on page 40 in Section 5.3

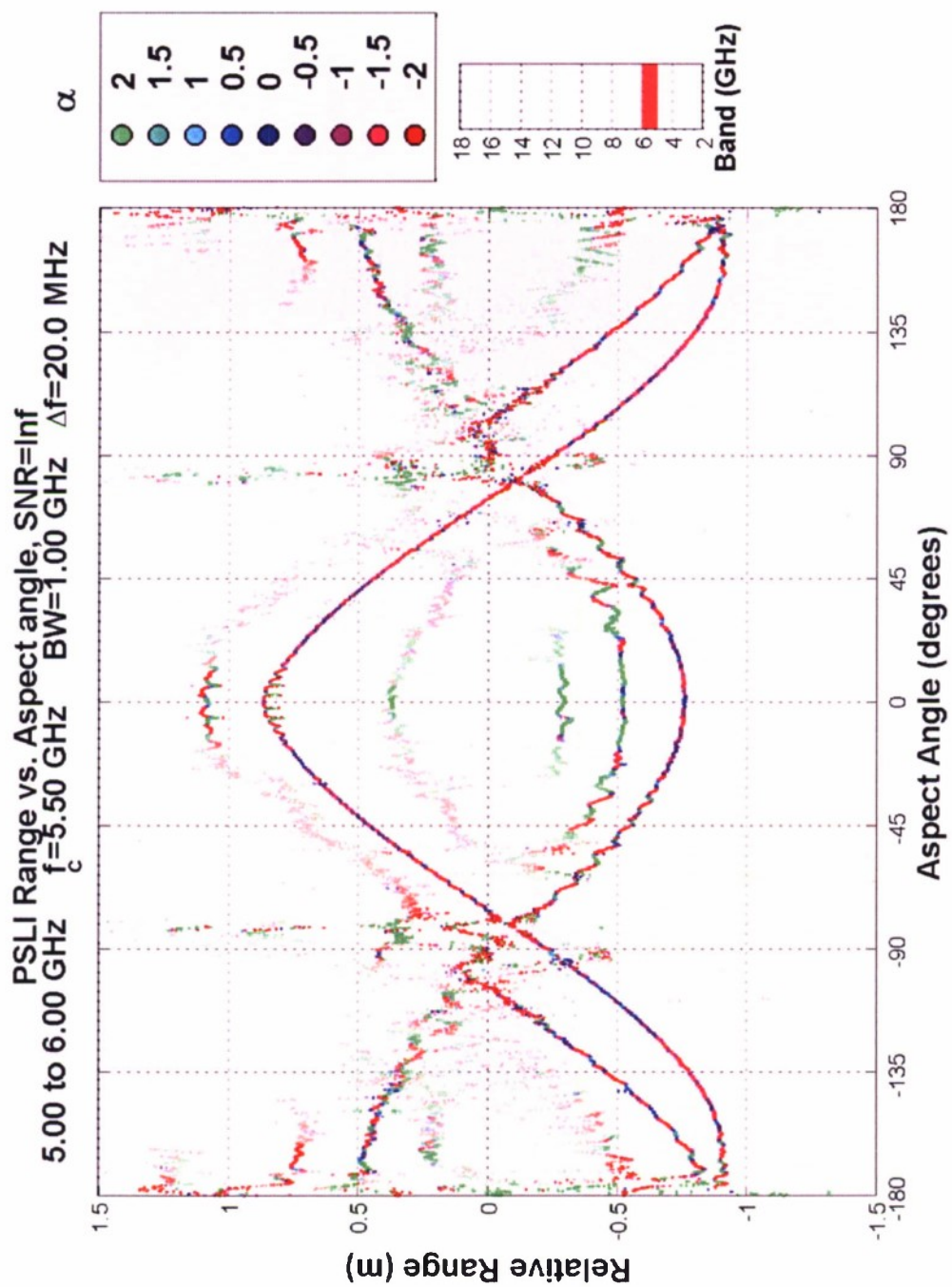


Figure A-4. C-Band, 1.00 GHz bandwidth, Description found with Fig. 29 on page 40 in Section 5.3

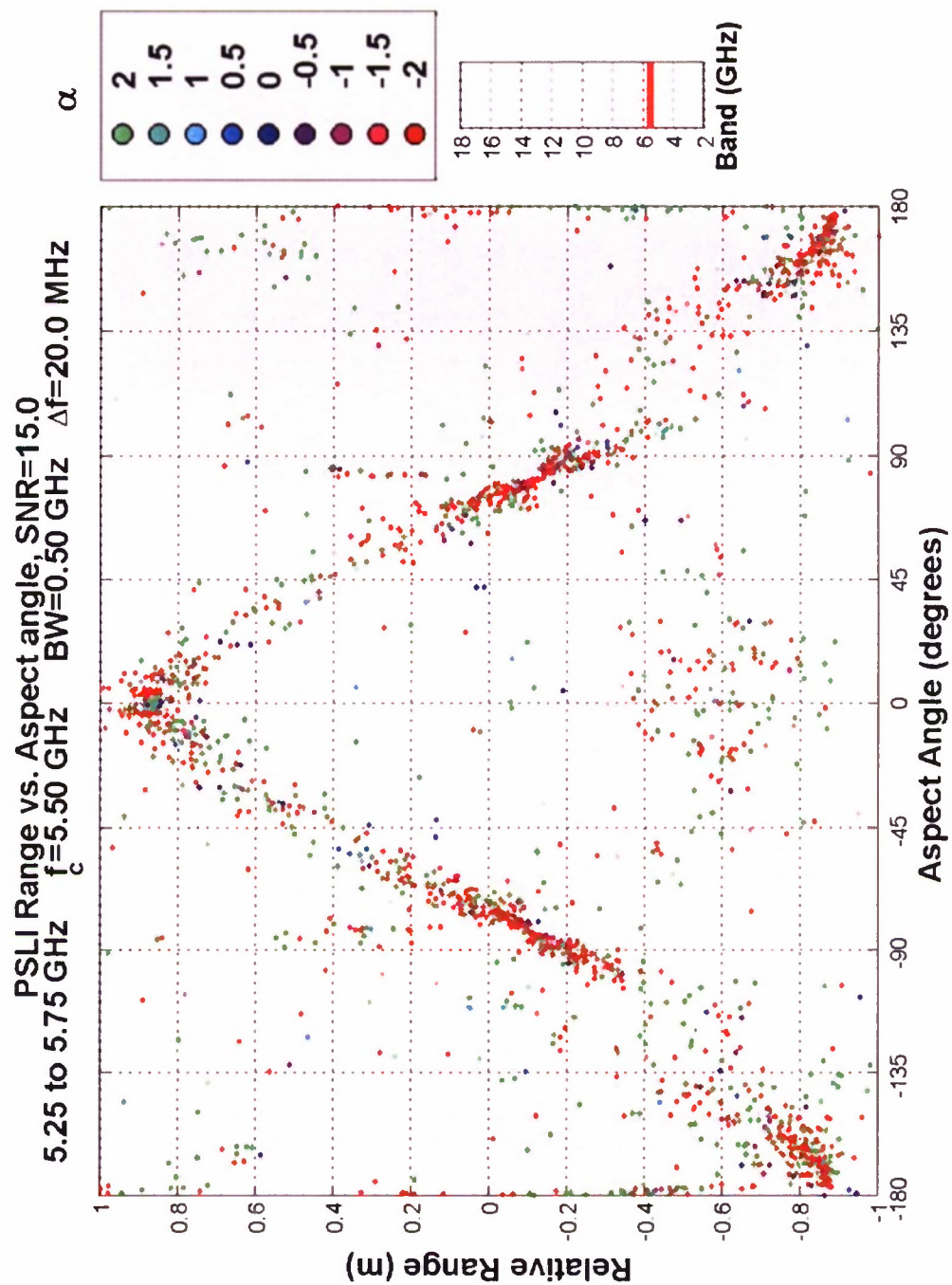


Figure A-5. C-Band, 0.50 GHz bandwidth, 15 dB SNR, Description found with Fig. 30 on page 40 in Section 5.3

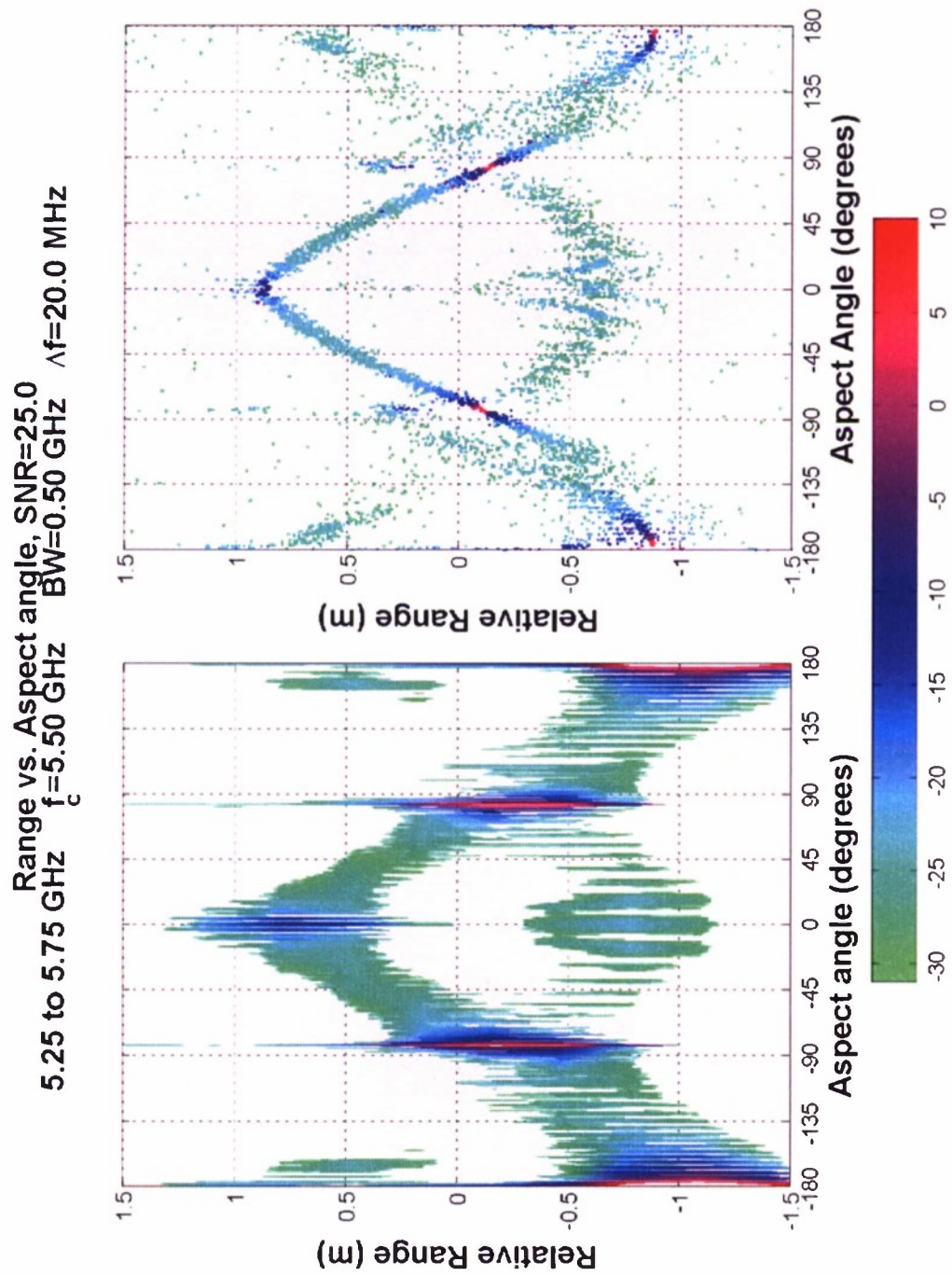


Figure A-6. Fourier vs. PSLLI, C-Band, 1.00 GHz bandwidth, 25 dB SNR, Description found with Fig. 31 on page 40 in Section 5.3

A.2 X-BAND

This section contains various figures with center frequencies of 10 GHz.

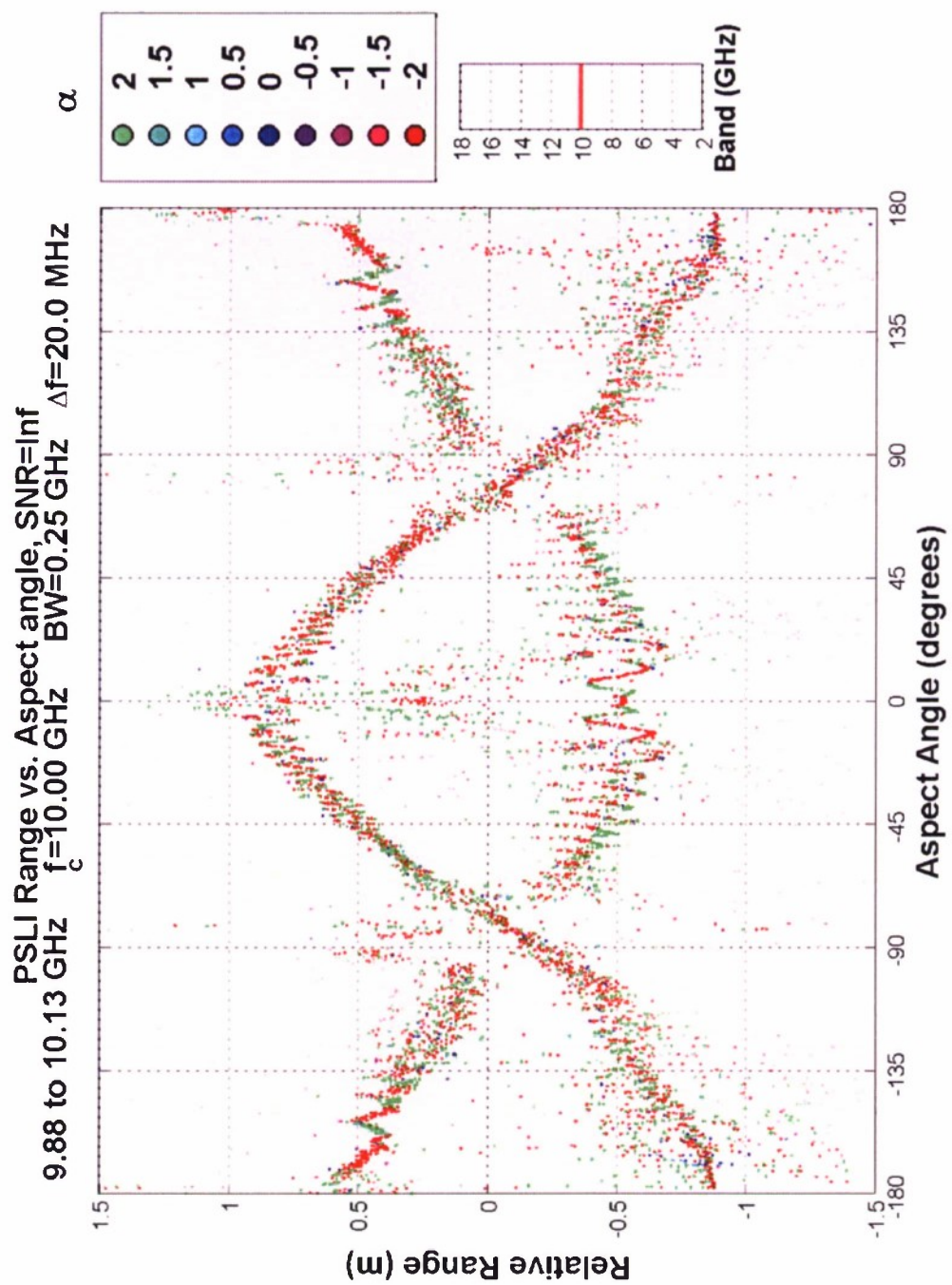


Figure A-7. X-Band, 0.25 GHz bandwidth, Description found with Fig. 25 on page 36 in Section 5.3

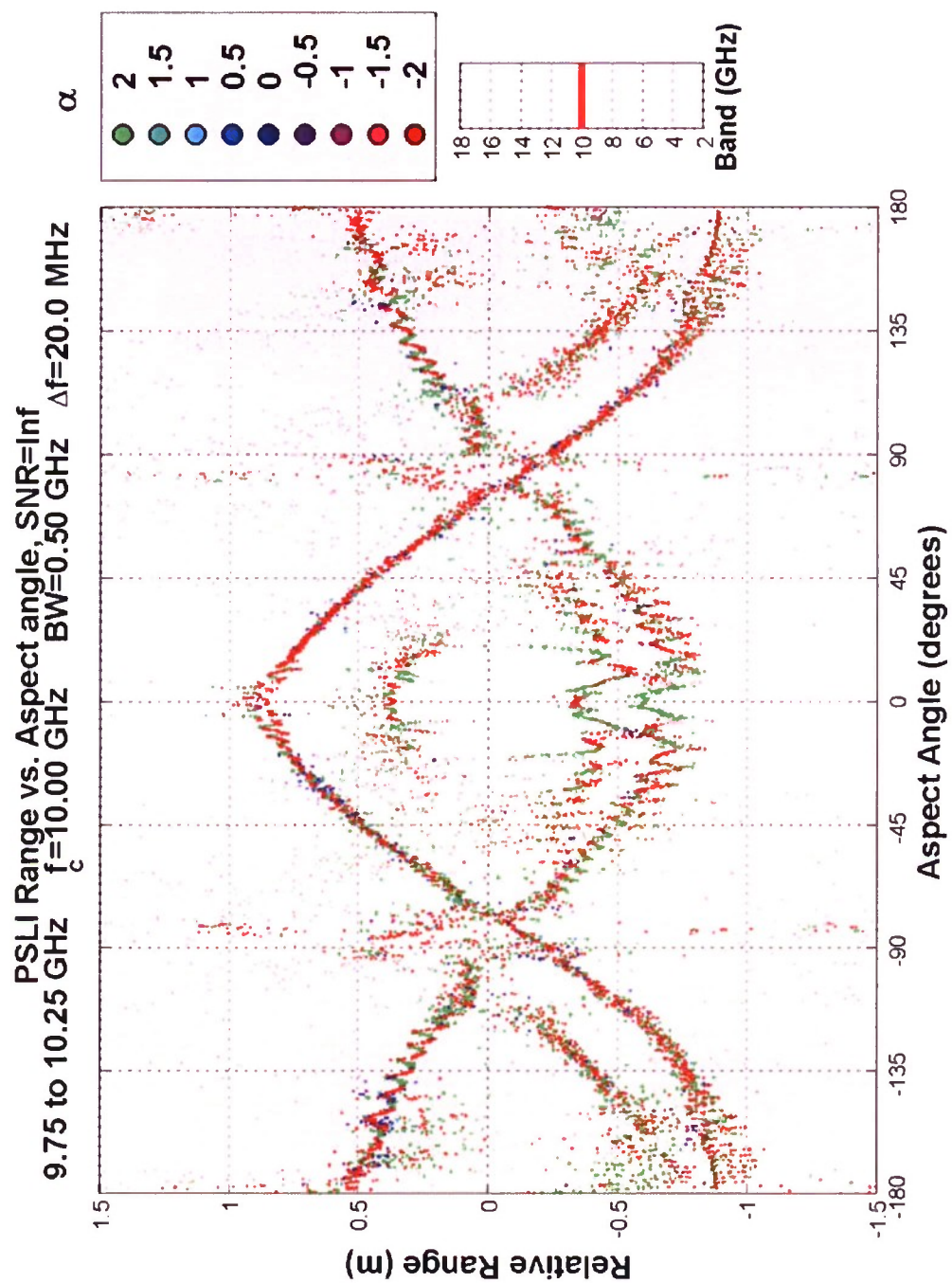


Figure A-8. X-Band, 0.50 GHz bandwidth, Description found with Fig. 26 on page 36 in Section 5.3

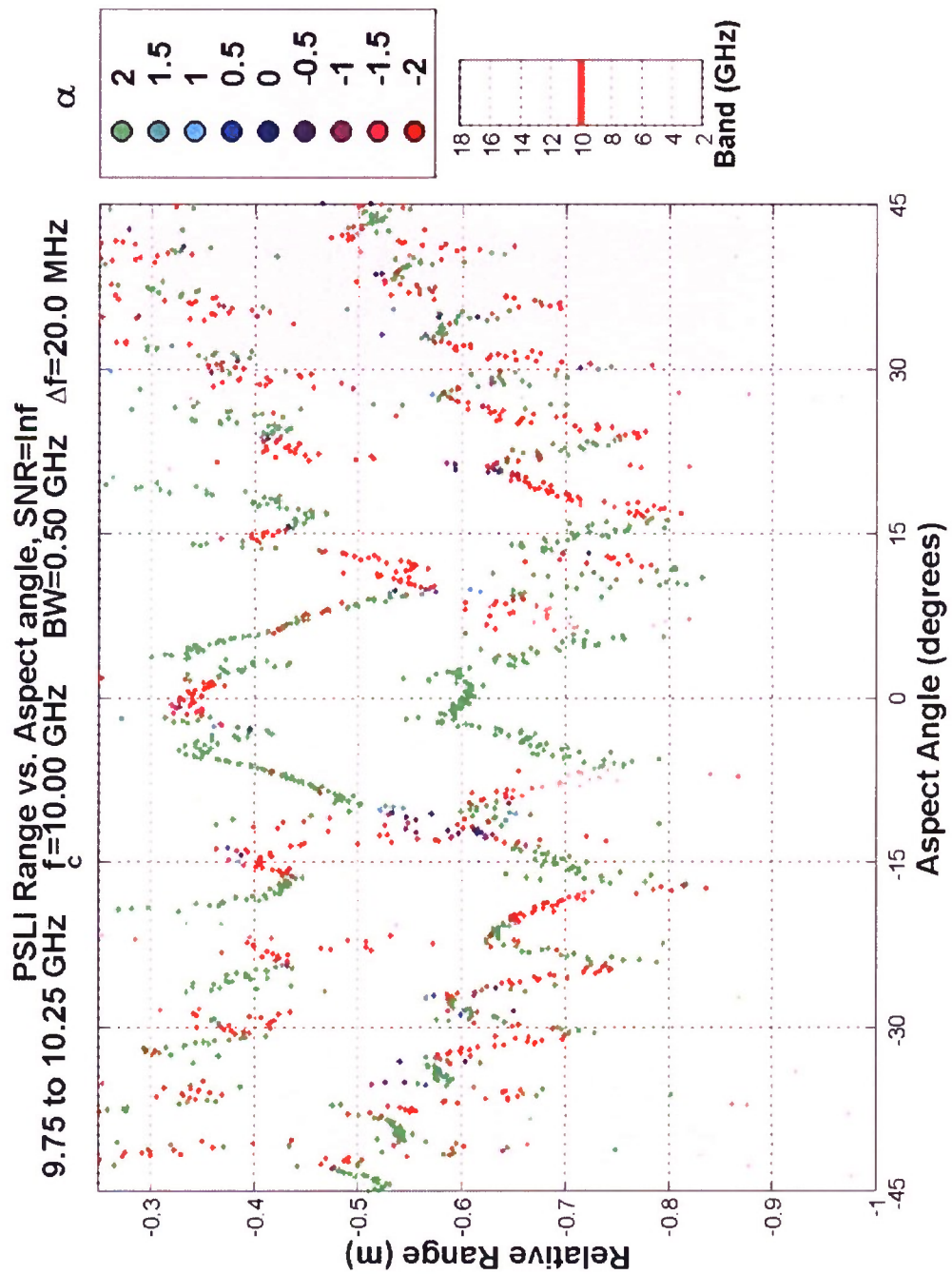


Figure A-9. X-Band, 0.50 GHz bandwidth, zoomed on the cone tip., Description found with Fig. 28 on page 40 in Section 5.3

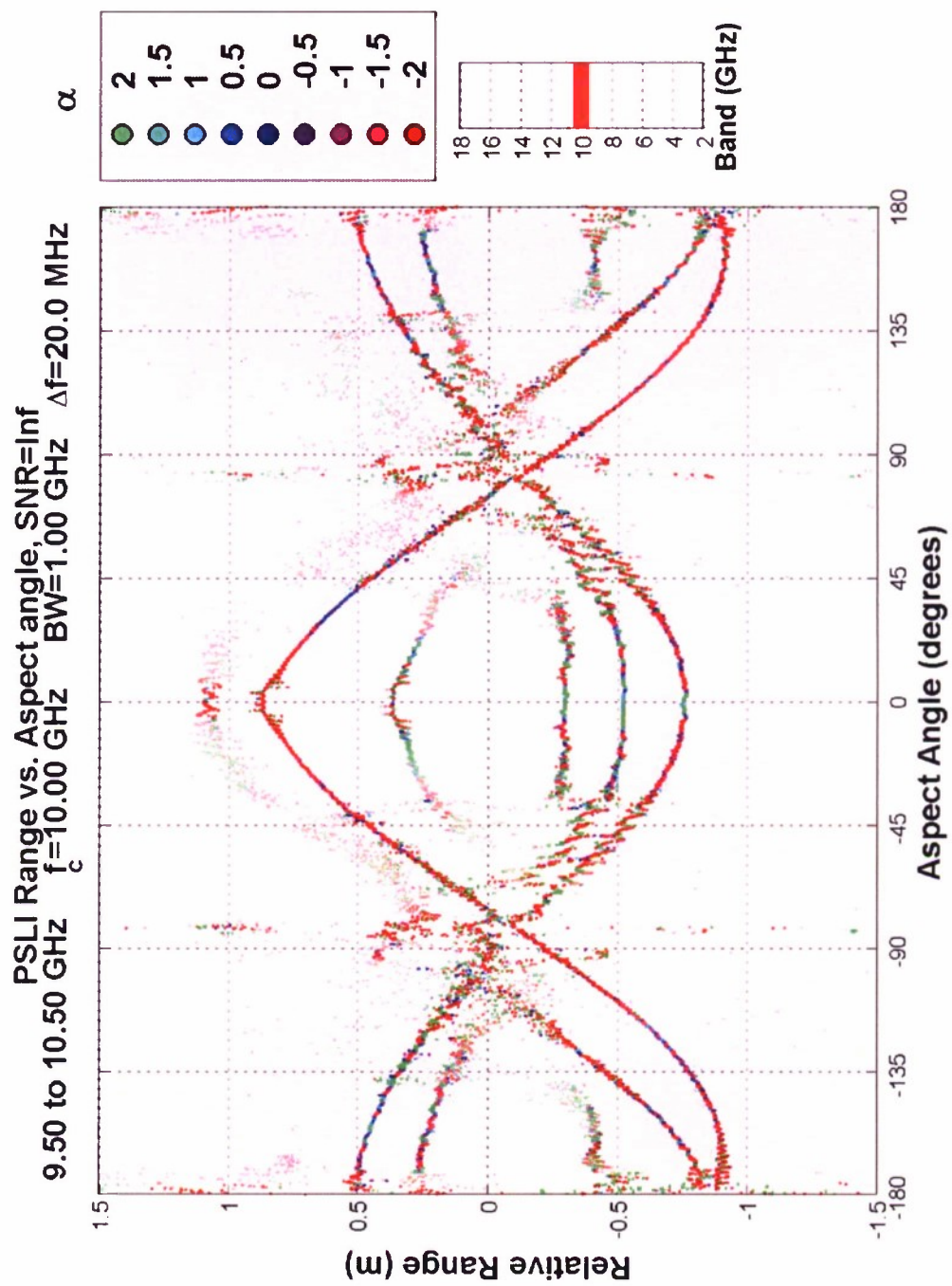


Figure A-10. X-Band, 1.00 GHz bandwidth, Description found with Fig. 29 on page 40 in Section 5.3

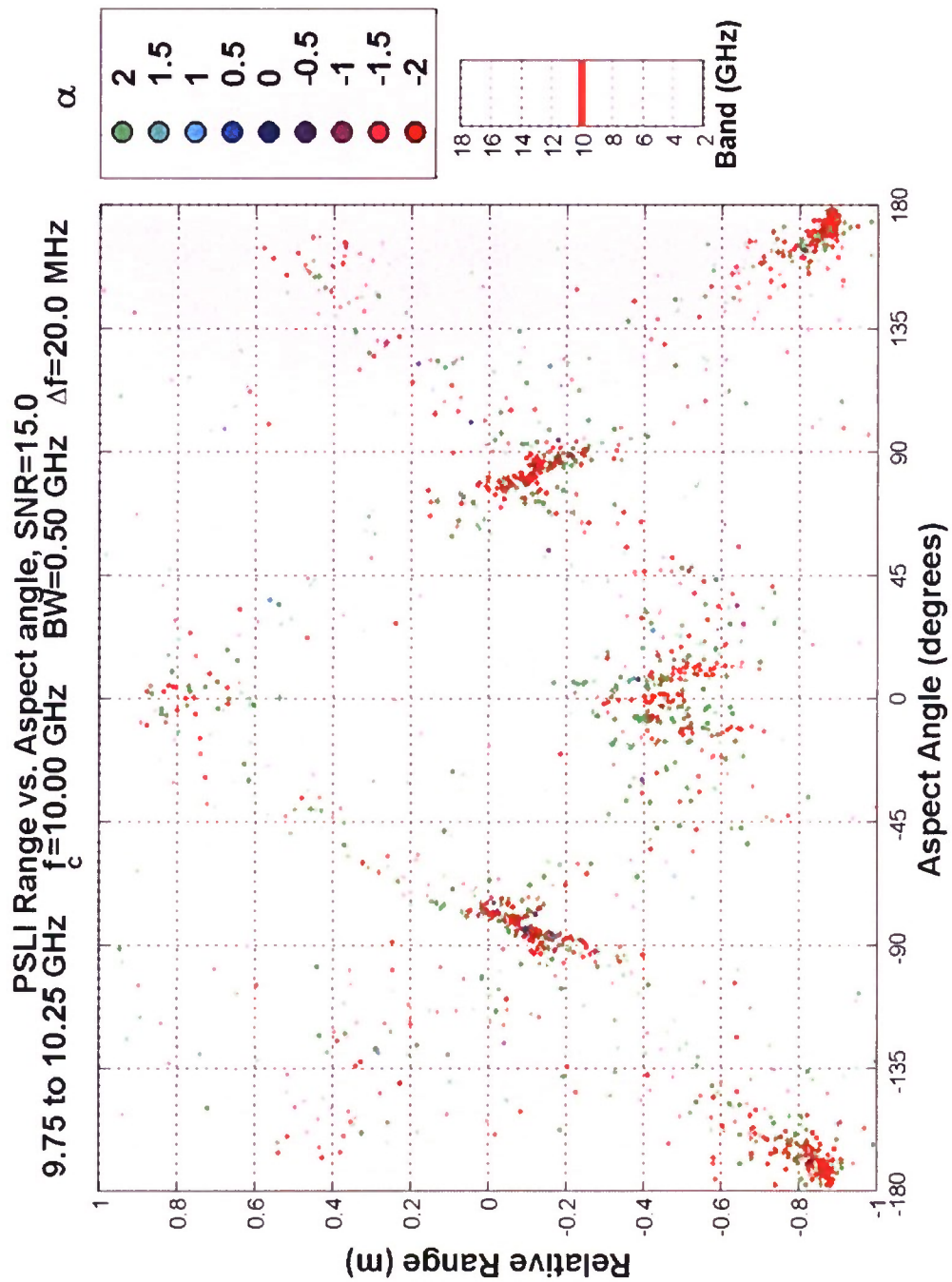


Figure A-11. X-Band, 0.50 GHz bandwidth, 15 dB SNR, Description found with Fig. 30 on page 40 in Section 5.3

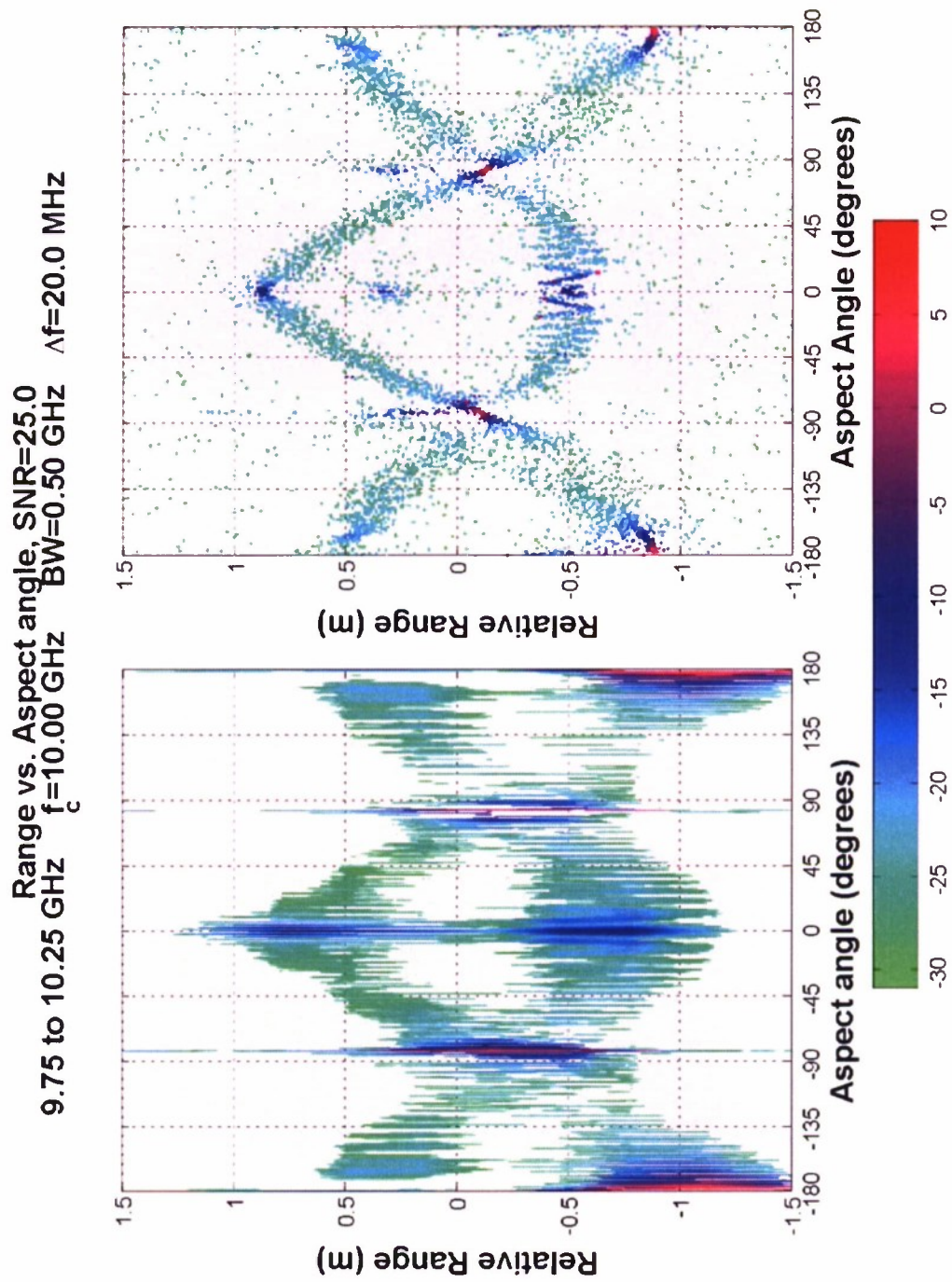


Figure A-12. Fourier vs. PSLL, X-Band, 1.00 GHz bandwidth, 25 dB SNR, Description found with Fig. A-12 on page 40 in Section 5.3

GLOSSARY

ATR	Automatic Target Recognition
CRB	Cramer-Rao Bound
DSS	Direct State Space Analysis
FIM	Fisher's Information Matrix
GTD	Geometric Theory of Diffraction
JNF	Jordan Normal Form
MSA	Modern Spectral Analysis
NEM	Nearest Exponential Model
PDF	Probability Density Function
PIPL	Positive Integer Power Law
PRF	Pulse Repetition Frequency
PSLI	Parametric Scattering Law Identification
RCS	Radar Cross Section
SNR	Signal-to-Noise Ratio
STM	State Transition Matrix
SVD	Singular Value Decomposition

REFERENCES

- [1] M. L. Burrows. Two-dimensional ESPRIT with tracking for radar imaging and feature extraction. Technical Report 1, January 2004.
- [2] Chi-Tsong Chen. *Linear System Theory and Design, 3rd Ed.*, pages 55–61. Oxford University Press, New York Oxford, 1999.
- [3] R. Corless and P. Giammi. A reordered Schur factorization method for zero-dimensional polynomial systems with multiple roots. pages 133–140. ISSAC '97, Maui Hawaii, 1997.
- [4] K. M. Cuomo, J. E. Piou, and J. T. Mayhan. Ultrawide-band coherent processing. *IEEE Transactions on Antennas and Propagation*, 47(6):1094–1107, June 1999.
- [5] James W. Demmel. *Applied Numerical Linear Algebra*, pages 140–153. SIAM, Philadelphia, 1997.
- [6] G.H. Golub and C.F. Van Loan. *Matrix Computations, 3rd Ed.*, page 324. The Johns Hopkins University Press, 1996.
- [7] G.H. Golub and V. Pereyra. The differentiation of pseudo-inverses and nonlinear least squares problems whose variables separate. *SIAM Journal of Numerical Analysis*, 10(2), April 1973.
- [8] B. Kagstrom and A. Ruhe. An algorithm for numerical computation of the Jordan normal form of a complex matrix. *ACM Transactions on Mathematical Software*, 6(3), September 1980.
- [9] J. Keller. Geometrical theory of diffraction. *Journal of the Optical Society of America*, 1962.
- [10] S.Y. Kung, K.S. Arun, and B.D. Rao. State space and svd based modeling methods for the harmonic retrieval problem. *Journal of the Optical Society Of America.*, 73(12):1799–1811, 1983.
- [11] Valentina Marotta. Resultants and neighborhoods of a polynomial. Hagenberg, Austria, September 1999. Symbolic and Numerical Scientific Computation, Second Intl. Conference, SNSC2001. Lecture Notes in Computer Science, 2630, Springer, 2003.
- [12] D. L. Mensa. *High Resolution Radar Cross-Section Imaging*, page 47. Artech House, Inc., 1991.
- [13] Fredy D. Neeser and James L. Massey. Proper complex random processes with applications to information theory. *IEEE Transactions on Information Theory*, 39(4):1293–1302, July 1993.
- [14] J. E. Piou, K. M. Cuomo, and J. T. Mayhan. A state-space technique for ultrawide-band coherent processing. (1054), July 1999.

- [15] L. Potter. A GTD-based parametric model for radar scattering. *IEEE Transactions on Antennas and Propagation*, 43(10):1058–1067, October 1995.
- [16] Bhaskar D. Rao and K. S. Arun. Model based processing of signals: A state space approach. *Proceedings of IEEE*, 80(2):283–309, February 1992.
- [17] G.W. Stewart and Ji guang Sun. *Matrix Perturbation Theory*, pages 174, Thm. 1.12. Academic Press, London, 1999.
- [18] Harry L. Van Trees. *Optimum Array Processing, Part IV of Detection, Estimation, and Modulation Theory*, pages 925–928. John Wiley & Sons, Inc., New York, 2002.
- [19] L. N. Trefethen. *Maxims about numerical mathematics, computers and life*.
- [20] J.H. Wilkinson. *Rounding Errors in Algebraic Processes*, page 39. Prentice-Hall, Englewood Cliffs, N.J., 1963.
- [21] RV model coating RCS measurements program, RCS test plan sphere-cone target. Technical Report F19628-95-C-002, CX-22751, MIT/LL, PT. Mugu, DynCorp: Aerotherm Corp., August 1999.
- [22] Z. Zeng. A method computing multiple roots of inexact polynomials. pages 266–272. ISSAC '03 Aug. 3-6, Philidelphia, August 2003.
- [23] Rodger E. Ziemer, William H. Tranter, and D. Ronald Farnin. *Signals and Systems: Continuous and Discrete, 3rd Ed.*, pages 523–524. Macmillan Publishing Co., New York, 1993.

REPORT DOCUMENTATION PAGEForm Approved
OMB No. 0704-0188

Public reporting burden for this collection of information is estimated to average 1 hour per response, including the time for reviewing instructions, searching existing data sources, gathering and maintaining the data needed, and completing and reviewing this collection of information. Send comments regarding this burden estimate or any other aspect of this collection of information, including suggestions for reducing this burden to Department of Defense, Washington Headquarters Services, Directorate for Information Operations and Reports (0704-0188), 1215 Jefferson Davis Highway, Suite 1204, Arlington, VA 22202-4302. Respondents should be aware that notwithstanding any other provision of law, no person shall be subject to any penalty for failing to comply with a collection of information if it does not display a currently valid OMB control number. **PLEASE DO NOT RETURN YOUR FORM TO THE ABOVE ADDRESS.**

1. REPORT DATE (DD-MM-YYYY) 26-04-2004		2. REPORT TYPE Technical Report		3. DATES COVERED (From - To)	
4. TITLE AND SUBTITLE Power-Law Scattering Models and Nonlinear Parametric Estimation for Super-Resolution				5a. CONTRACT NUMBER F19628-00-C-0002	
				5b. GRANT NUMBER	
				5c. PROGRAM ELEMENT NUMBER	
6. AUTHOR(S) N. Hatch, D. Holl, Jr., D. Cyganski				5d. PROJECT NUMBER	
				5e. TASK NUMBER	
				5f. WORK UNIT NUMBER	
7. PERFORMING ORGANIZATION NAME(S) AND ADDRESS(ES) MIT Lincoln Laboratory 244 Wood Street Lexington, MA 02420-9108				8. PERFORMING ORGANIZATION REPORT NUMBER TR-1095	
9. SPONSORING / MONITORING AGENCY NAME(S) AND ADDRESS(ES) HQ ESC/XPB 5 Eglin St. Hanscom AFB, MA 01731-2100				10. SPONSOR/MONITOR'S ACRONYM(S) ESC/XPB	
				11. SPONSOR/MONITOR'S REPORT NUMBER(S) ESC-TR-2004-075	
12. DISTRIBUTION / AVAILABILITY STATEMENT Approved for public release; distribution is unlimited.					
13. SUPPLEMENTARY NOTES					
14. ABSTRACT This paper introduces a direct solution of the frequency-dependent, GTD-based, scatterer model parameters leading towards a new modern spectral estimation technique to be used for enhanced superresolution RADAR analysis. The overcomplete nature of the full GTD scatterer model basis (positive and negative half-integer power laws) is recognized and overcome by introducing the vector channel method, well known from communication theory. This physically motivated discrete-model based analysis eliminates the need for computationally intensive and potentially non-convergent local optimization procedures. Each scatterer is assigned a half-integer power law that identifies its cross section frequency dependence and hence restricts the possible underlying physical feature geometries. This analysis opens the possibility for vector-attribute based feature processing for target recognition that offers the potential for significant improvement in target identification performance.					
15. SUBJECT TERMS					
16. SECURITY CLASSIFICATION OF:			17. LIMITATION OF ABSTRACT None	18. NUMBER OF PAGES 70	19a. NAME OF RESPONSIBLE PERSON
a. REPORT Unclassified	b. ABSTRACT Unclassified	c. THIS PAGE Unclassified			19b. TELEPHONE NUMBER (include area code)